Atmos. Chem. Phys., 26, 3167–3184, 2026
https://doi.org/10.5194/acp-26-3167-2026
© Author(s) 2026. This work is distributed under
the Creative Commons Attribution 4.0 License.

Atmospheric Chemistry and Physics
Open Access
EGU

Concentration and size distribution of black carbon over the ablation area of Potanin glacier: enrichment ability of surface weathering granular ice of water-insoluble particles with snow/ice melting

Sayako Ueda[1], Akiko Sakai[1], Sho Ohata[2], Purevdagva Khalzan[3], Sumito Matoba[4], Ken Kondo[1], and Hitoshi Matsui[1]

[1]Graduate School of Environmental Studies, Nagoya University, Furo-cho, Chikusa-ku, Nagoya 464-8601, Japan
[2]Institute for Space–Earth Environmental Research, Nagoya University, Nagoya, 464-8601, Japan
[3]Information & Research Institute of Meteorology Hydrology & Environment, Ulaanbaatar 15160, Mongolia
[4]Institute of Low Temperature Science, Hokkaido University, Sapporo 060-0819, Japan

Correspondence: Sayako Ueda (ueda.sayako.u2@f.mail.nagoya-u.ac.jp)

Received: 27 October 2025 – Discussion started: 12 November 2025
Revised: 5 February 2026 – Accepted: 16 February 2026 – Published: 3 March 2026

Abstract. Light-absorbing particles on surface ice in ablation areas can accelerate glacier melting and shrinkage. A Single Soot Particle Photometer was used to measure black carbon (BC) mass concentrations (M_{BC}) in the ablation area of Potanin Glacier, Mongolia during summer. Surface-ice M_{BC} values (42–555 ng g^{-1}) greatly exceeded those of surface snow (5–22 ng g^{-1}), snow and rain (2–6 ng g^{-1}), and surface melt water (2–11 ng g^{-1}). Vertical profiles of M_{BC} revealed high surface-layer concentrations, suggesting impurities trapped in the granular ice: the particularly low-density layer of the weathering crust surface. In the ablation area, M_{BC} values of granular ice decreased with lower elevation: 134–601 ng g^{-1} at the 3317 m site and 8–96 ng g^{-1} at the 3078 m site. The fraction of residual surface BC to BC contained in lost water over a year, R, was calculated using the yearly BC deposition flux and water ablation weight A_w. Average R values were 0.17 and 0.011, respectively, at 3317 and 3078 m. A_w were 246 and 325 g w.e. cm^{-2}, suggesting that the granular ice retains BC particles best in the upstream ablation area, showing concomitantly less capability with increasing ablation. Enriched BC on the ablation area surface comprises recent BC deposits and BC from the glacier's lower layer after rising during decades or more. Those BC emissions and deposits can therefore affect both future and present ablation area melting processes.

1 Introduction

Black carbon (BC) is emitted into the atmosphere through combustion activities such as burning fossil fuels and biomass. The light absorption properties of BC can influence the Earth's radiation budget strongly through atmospheric processes and positive feedback on snow and ice albedo, consequently exacerbating the melting of snow and ice after deposition on surfaces (e.g. Bond et al., 2013; Hansen and Nazarenko, 2004; Mori et al., 2019; Ramanathan and Carmichael, 2008; Skiles et al., 2018). Because of global warming, the area covered by mountain glaciers has been shrinking in recent years (Hugonnet et al., 2021; Khalzan et al., 2022; The GlaMBIE Team, 2025). Over decades, glaciers flow from high-altitude accumulation areas, where temperatures are below freezing, to low-altitude ablation areas (Cuffey and Paterson, 2010). At ablation areas, surface snow and ice melt and flow out through water channels, either

into or over the glacier. Understanding the relation between snowmelt and light-absorbing particles in ablation areas is necessary for comprehension of glacier shrinkage processes.

Most glacier studies have used thermal–optical carbon analysis (e.g. Li et al., 2017, 2018; Zhang et al., 2017, 2020). By contrast, although used only rarely for glacier studies (Kaspari et al., 2014; Konya et al., 2021; Marquetto et al., 2020), nebulizer and Single Soot Particle Photometer (SP2) systems have been applied for BC measurements supporting ice core and snow research (Bisiaux et al., 2012a, b; Goto-Azuma et al., 2024, 2025; Kaspari et al., 2011; McConnell et al., 2007; Mori et al., 2016, 2019, 2020; Osmont et al., 2018; Sinha et al., 2018; Sigle et al., 2018; Sterle et al., 2013). Unlike the thermal–optical method, which measures particles accumulated in a filter sample, the SP2, an aerosol measuring instrument, counts individual BC particles and their mass individually. The resultant count provides a size–number/mass distribution of BC, which is useful for elucidating particle dynamics and albedo. The SP2 in wide-range mode, which replaces the detector used to measure the aerosol shell with one that measures large BC particles, can measure BC, including large particle sizes that the standard SP2 is unable to detect (Mori et al., 2016).

Several earlier glacier reports have described concentrations of BC and other impurities such as mineral dust and organic matter (OM). Thermal–optical measurements of BC have often been used to assess BC levels around the Tibetan Plateau, where concentrations higher than $1000\,\mathrm{ng\,g^{-1}}$ have been reported (Li et al., 2017, 2018; Ming et al., 2016; Qu et al., 2014; Xu et al., 2012; Zhang et al., 2017, 2020). Based on measurements of impurities on glaciers, surface albedo has also been estimated, suggesting that BC can contribute to reduction of albedo in some places (Zhang et al., 2020). The mass concentration of BC in aged snow tends to be higher than in fresh snow. It consequently increases with lower elevation over the accumulation glacial area (Li et al., 2017, 2018; Zhang et al., 2017, 2020), suggesting BC enrichment over snow surfaces. The enrichment with impurities is attributed to sublimation, evaporation, and snow melting (Aoki et al., 2014; Doherty et al., 2013; Kuchiki et al., 2015; Ming et al., 2016; Qu et al., 2014; Xu et al., 2012). Nevertheless, quantitative discussions of enrichment and the principles of enrichment in melting warrant support based on further research. Particularly, observational studies addressing ablation areas affected by intense melting are few. Consequently, factors affecting BC concentrations and contributing to melting over the glacier surface in the ablation area remain unclear.

For this study, we collected snow and ice samples from the Potanin Glacier in Mongolia, located in the East Asian high mountain range, with particular examination of the ablation area. BC mass concentrations and size distributions were measured using a wide-range SP2. Observations were conducted during the summer (July–August) of 2022 for vertical profiles, in 2023 for different snow and ice samples (precipitation, snow, ice, and water over the glacier surface), and in 2024 for altitude differences of surface granular ice (the low-density surface layer of the weathering crust, which can be readily sampled using a shovel). Based on the observed BC concentrations, one can infer the enrichment process of BC particles over the surface ice of the glacier ablation area. Furthermore, this study demonstrates and evaluates a method for quantitative estimation of the residual ability of BC particles in surface granular ice at each location.

2 Field Observations and Laboratory Methods

2.1 Observation site and sampling

Potanin Glacier is located in the Tavan Bogd region, which lies along the border separating Mongolia, Russia, and China. The Tavan Bogd region, which is designated as a national park, is protected from residential development, making it a particularly popular tourist destination. Potanin Glacier, which flows from the summit of Mt. Khuiten (4374 m above sea level (a.s.l.)), is the highest peak among the Altai Mountains situated eastward. The glacier extends 10.4 km along a valley and terminates at 2907 m a.s.l. (Fig. 1). The glacier area is estimated as $24.7\,\mathrm{km^2}$. The surrounding terrain is not steep. The ablation area of this glacier has a gentle slope (about 7°). Its mass balance has been observed using stakes at 50–100 m elevation intervals on the Potanin (14 stakes), as described by Khalzan et al. (2022, 2025). For this study, surface snow was collected along with ice or water samples from around four stakes (st5r, 4c, 3c, and 2c) that were located at the midpoint of each elevation and at the accumulation area point (ACC) shown in Fig. 1. Details of each stake are presented in Table 1. The glacier flow velocity was measured by application of feature tracking (Sakakibara and Sugiyama, 2014, 2020) to image pairs of Landsat 9 images acquired on 28 July 2022 and 31 July 2023. We used an automatic image matching scheme known as the orientation correlation method in a frequency domain (Heid and Kääb, 2012; Sakakibara and Sugiyama, 2020). Horizontal biases in the image pair were corrected by minimizing displacement vectors over ice-free areas. Vectors with a low signal-to-noise ratio (< 30) and those deviating by more than 30° or $100\,\mathrm{m\,a^{-1}}$ from the median vector within 3×3 neighboring pixels were excluded from analyses. Errors in the velocity measurement were estimated as $\pm 1.7\,\mathrm{m\,a^{-1}}$ based on results obtained for stable ice-free areas.

Figure 2 presents an example of a sampling site. Meltwater flowed through channels on the glacier's surface in the ablation area. On 12 July 2023, the glacier was covered in white aged snow, which by 8 August had melted away and had exposed weathering crust covered with granular ice layer at the surface after experiencing some melting and refreezing. Weathering crust over st5r, 4c, 3c, and 2c were dark compared to the snow-covered surface. Colored impurities were clearly concentrated in the granular ice on the surface

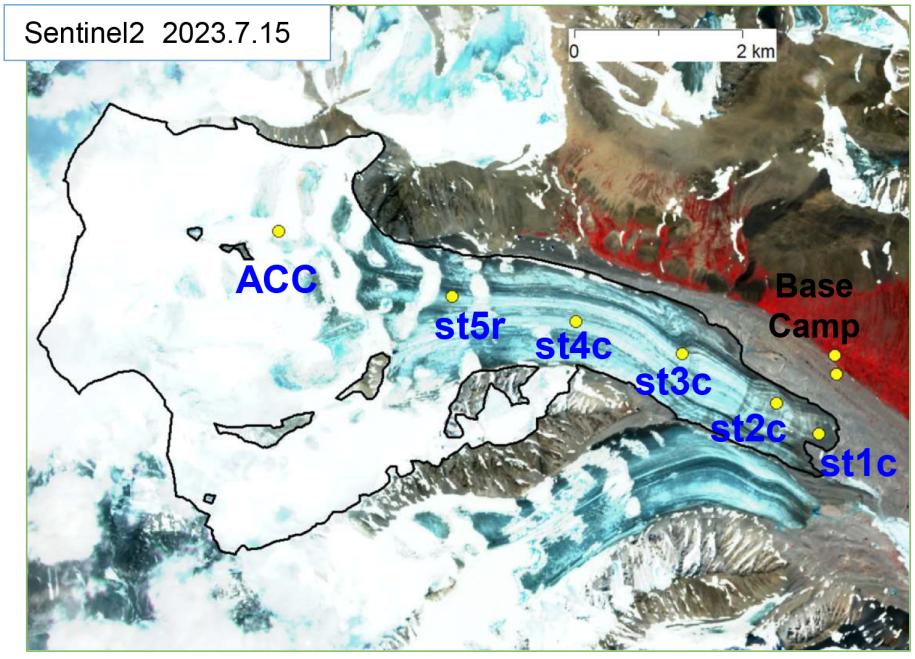

Figure 1. Satellite photograph of Potanin Glacier and locations of stakes.

Table 1. Elevations for each stake, glacier flow velocity, and atmospheric temperature and ice temperature of ACC, st5r, st4c, st3c, and st2c sites.

	Elevation [m a.s.l.]	Glacier flow velocity	Atmospheric temperature [°C]	Ice temperature [°C]		
		[m yr^{-1}]	Avg. [Min.–Max.]	−20 cm	−50 cm	−100 cm
ACC	3757	n/a	n/a	n/a	n/a	n/a
t5r	3317	59	4.2 [−0.5–12.1] (12 Jul–11 Aug 2023)	0.03	−0.6 (2 Jul 2023)	−1.7
St4c	3232	27	n/a	n/a	n/a	n/a
St3c	3150	1.5	n/a	n/a	n/a	n/a
St2c	3078	1.0	6.3 [1.3–11.8] (12 Jul–11 Aug 2023)	0.03	−0.8 (3 Jul 2023)	−2.0

n/a: not applicable

of the weathering crust layer. Snow, ice and water samples were collected according to the following classification: surface snow, surface ice (i.e. the surface granular ice), surface water (i.e. meltwater) and precipitation (i.e. snow and rain). These samples are listed in Tables S1–S4 in the Supplement. Using a stainless steel scoop, snow and ice samples about 10 cm × 10 cm area were collected in dust-free plastic bags. After melting the snow and ice in the plastic bags under ambient temperature (about 7 °C) at base camp, the resulting liquid was stored in 30 or 50 mL glass bottles (SV30 and SV50; Nichiden Rika Glass Co., Ltd.) for BC measurements. Some samples were collected in 10 mL PET vials (JST-R/N10 and JST-R/N30; Nikko Hansen & Co., Ltd.) for TEM analysis. Surface water was collected directly in glass bottles. Precipitation samples were collected in dust-free plastic bags over a basin at the base camp. In 2023, we collected samples, particularly addressing different snow types. In 2024, we collected multiple samples around each stake to obtain statistical data of the surface granular ice considering the spatial discrepancy of samples. In 2022, 4.2 and 3.0 m ice core samples were collected at st2c on 31 August and at st3 on 1 September. Based on our earlier evaluation of storage methods (Ueda et al., 2025), BC mass concentrations were obtainable from liquid samples stored at approximately 4 °C that were comparable to freshly melted samples. However, refreezing can lead to a considerably large (> 20 % on average) loss. Therefore, the samples were kept liquid and were transported to

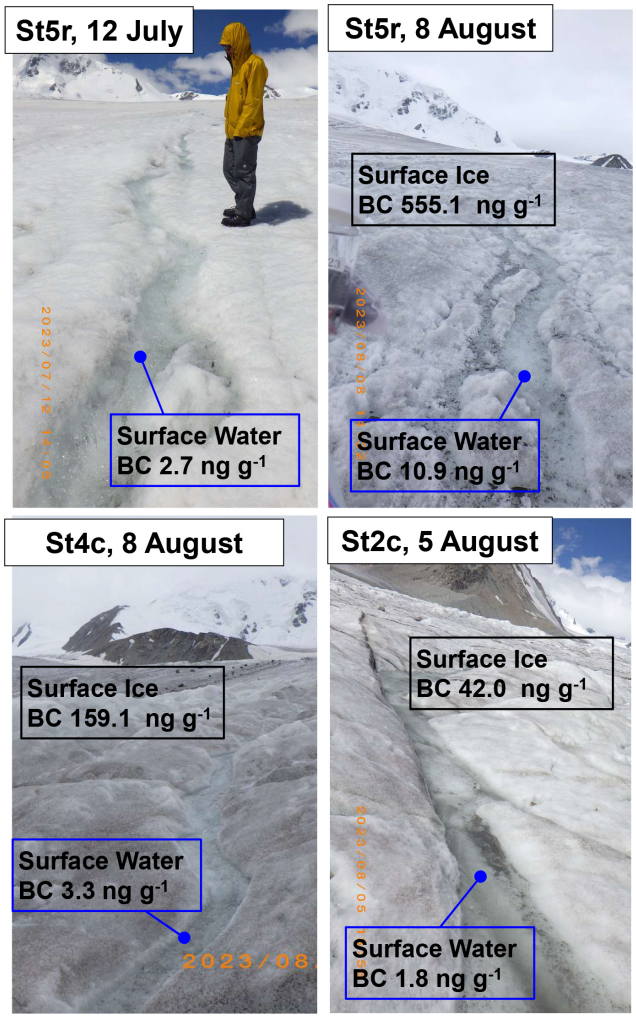

Figure 2. Examples of sampling site views, 2023, and the BC mass concentrations.

Nagoya University by refrigerated delivery. There they were stored at 4 °C until measurement.

2.2 BC measurement using a nebulizer–SP2 system

The mass and number size distributions of BC in liquid samples were measured using a system consisting of a pneumatic nebulizer (Marin-5; Cetac Technologies Inc., USA) and the SP2 (Mori et al., 2016, 2019, 2020, 2021; Sinha et al., 2018). Details of the measurement system used for this study were described by Ueda et al. (2025). Liquid samples were injected into the nebulizer at a constant flow rate of 0.18 mL min^{-1} to be aerosolized with 0.8 L min^{-1} clean compressed air. Some aerosolized particles were subsequently introduced into the SP2 at a flow rate of 0.12 L min^{-1}. The SP2 detects individual BC particles from their incandescence signals and BC-free particles from their light-scattering signals in the carrier gas. A standard SP2 measures the mass of each BC particle with mass equivalent diameter (D_{BC}) within the 70–850 nm range by assuming BC particle density of 1.8 g cm^{-3} (Moteki and Kondo, 2010), whereas the SP2 used for this study measures masses of BC particles within the 70–3000 nm range by expanding the upper limit of the detected incandescence signal in the standard SP2 (Mori et al., 2016). Because the FeO_x in such as dust also radiates incandescence, the BC concentration by SP2 was calculated excluding FeO_x detection by referencing the ratio of red-band to blue-band incandescence signals (Mori et al., 2023; Yoshida et al., 2016). The number concentration (N_{BC}) and mass concentration (M_{BC}) of BC in water for the 70–3000 nm diameter range were derived from the flow rates of the liquid sample and the carrier gas for the nebulizer, the nebulizer efficiency, and the measured size distribution of BC in the carrier gas.

Before measurement using the nebulizer-SP2 system, liquid samples in glass vials were sonicated for 10 min to minimize loss of BC that is unable to pass through the nebulizer system, such as BC attached to the vial wall and BC on the coarse particles. From many glacier samples in this study, turbidity and large dust particles were found. To prevent clogging of the nebulizer-SP2 system, after settling of large dust particles during standing for 10 min after sonication, suspended liquid samples in vial middles were dispensed into 10 mL PET vials (JST-R/N10; Nikko Hansen & Co., Ltd.). Then they were measured using the nebulizer-SP2 system. At the dispensing, samples were diluted 3–10 times using Milli-Q water according to their turbidity.

2.3 Mineral dust and water-insoluble organic matter

All samples used to measure mineral dust and water-insoluble organic matter were put into plastic bags, including all surface granular ice layer samples with impurities. After taking samples, we measured the sampled square area (length and width) and the sampling depth at four points of the sides of the sample square: the thickness of surface granular ice layer in the surface part of the weathering crust. The plastic bag was brought to the base camp. All ice was melted during 1 d, along with deposited impurities. All of the deposited impurities were put into 30 mL plastic bottles with formalin (1 % of samples). Using samples sent to the laboratory, mineral dust and water-insoluble organic matter were measured according to the method reported by Takeuchi and Li (2008), as modified from Dean (1974). The samples were dried at 60 °C for 24 h in pre-weighed crucibles. Then we ascertained the dried impurity amounts (mineral dust and organic matter) of samples. After removing the organic matter from dried samples by combustion at 500 °C for 3 h in an electric furnace, the weight of combusted samples was measured as mineral dust. We found the amount of organic matter from the difference in weight between the dried and combusted samples. Then, the amounts of mineral and organic matter per area were obtainable using the area measured when the samples were collected.

2.4 TEM analyses

Particles nebulized by Marin-5 from liquid samples in 10 mL PET vials were collected using a three-stage cascade impactor (50 % cutoff aerodynamic diameters of the two stages were 1 and 0.3 µm at a 0.5 L min^{-1} flow rate) on the TEM grid. Particles were collected on carbon-coated nitrocellulose (collodion) films over a Cu TEM grid (H7, 400 mesh, Reference Grids; Graticules Optics Ltd., UK). A water dialysis technique (Mossop, 1963; Okada, 1983; Ueda et al., 2011a, b) was used to remove water-soluble materials from the samples. The TEM grid with particle samples was floated on an ultrapure water drop (approximately 0.3 mL) on a Petri dish at about 40 °C for 3 h with the collection side upward. To avoid charging up and to obtain the height information of individual particles on the collection surface, particles were coated with a Pt/Pd alloy at a shadowing angle of 26.6° (arctan 0.5) before being micrographed. After water dialysis, residue materials on the TEM grid were photographed using TEM (JEM 2100-plus; JEOL, Japan) with 200 kV accelerating voltage. Elemental mapping was done using EDS (EX-24200M1G2T; JEOL Ltd., Japan) with TEM in scanning TEM (STEM) mode and 200 kV accelerating voltage. Elemental mapping data were obtained and analyzed using software (NSS 3; Thermo Fisher Scientific Inc., USA).

2.5 Global model simulation

BC deposition over the observation site was estimated using global model simulations with the Community Atmosphere Model ver. 5 coupled with the Aerosol Two-dimensional bin module for foRmation and Aging Simulations (CAM-ATRAS) (Matsui, 2017; Matsui and Mahowald, 2017; Matsui et al., 2018). This model incorporates a comprehensive set of aerosol and atmospheric processes, including emissions, gas-phase chemistry, condensation and evaporation of inorganic and organic species, coagulation, nucleation, aerosol activation and in-cloud processing, dry and wet deposition, and interactions with radiation and clouds. Aerosols are represented using 12 dry diameter bins of 1–10 000 nm. Eight BC mixing states are considered for particles of 40–1250 nm: BC-free, pure BC, and internally mixed BC-containing particles of six types.

Simulations were conducted for 2013–2023, with analyses particularly addressing 2014–2023. The model was run at a horizontal resolution of 1.9° × 2.5°, with 30 vertical layers extending up to approximately 40 km. Anthropogenic emissions were based on the Community Emissions Data System 2021 inventory (O'Rourke et al., 2021) and were assumed to be constant at 2019 levels for 2020–2023 because the inventory is available only through 2019. Sea surface temperatures and the sea ice extent were prescribed according to an earlier report by Hurrell et al. (2008). Horizontal winds and temperature in the free troposphere (above 800 hPa) were nudged toward the Modern-Era Retrospective analysis for Research and Applications ver. 2 reanalysis.

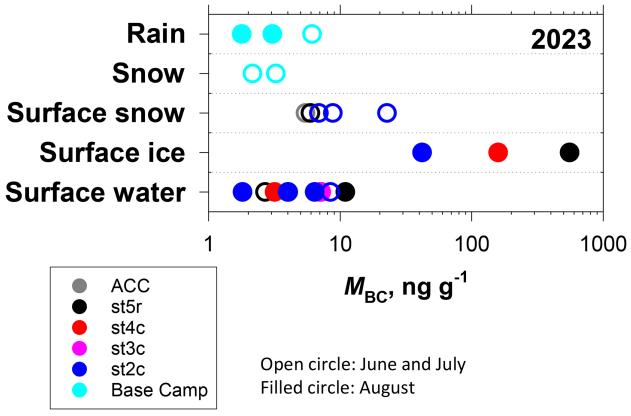

Figure 3. Mass concentrations of BC in water (M_{BC}) for surface snow, surface ice, surface water, snow, and rain samples collected during 30 June–12 August in 2023.

Against ground-based, aircraft, and satellite observations, CAM-ATRAS has been evaluated extensively. It has shown good agreement with observed BC concentrations at the surface, in vertical profiles, and on a global scale (e.g., Liu and Matsui, 2021a, b; Matsui and Mahowald, 2017; Matsui et al., 2022).

3 Results and Discussion

3.1 BC and other impurities over the ablation area

3.1.1 BC concentrations in snow, surface ice, water, and precipitation, 2023

Figure 3 presents the mass concentrations of BC in water (M_{BC}) found for surface snow, surface ice, surface water, snow, and rain samples collected in 2023. Some M_{BC} values are shown in Fig. 2. The M_{BC} values of precipitation (i.e., snow and rain) were 2–6 ng g^{-1}. The M_{BC} values of surface snow were 5–22 ng g^{-1}: slightly higher than those of precipitation. The values of surface ice were especially high, 42–555 ng g^{-1}, with a maximum value found for st5r. Surface water originates from the melt of surface snow and ice. However, the M_{BC} values for surface water were 2–11 ng g^{-1}, which are considerably lower values than those found for surface ice. The value found for st5r in July, when surface snow covered the area, was low: 3 ng g^{-1}. However, when surface granular ice (surface ice) came to be exposed in August, the value at st5r was highest among surface water, 11 ng g^{-1}, but it was sufficiently lower than that for surface ice: 555 ng g^{-1}.

The concentrations of BC on the surfaces of East Asian glaciers reportedly have widely variant values: from less than 10 ng g^{-1} to greater than 1000 ng g^{-1} (Li et al., 2017, 2018; Ming et al., 2016; Qu et al., 2014; Xu et al., 2012; Zhang et al., 2017, 2020). In fact, BC concentrations higher

than 3000 ng g^{-1} were observed for granular ice in the Xiao Dongkemadi glacier of the Tibetan Plateau (Li et al., 2017). In general, the concentrations of impurities (e.g. BC, mineral dust, and OM) tended to be higher in aged snow and in surface granular ice than in fresh snow over the accumulation glacial area (Li et al., 2017, 2018; Ming et al., 2016; Qu et al., 2014; Zhang et al., 2017, 2020). Sublimation and evaporation can condense the impurities which are present in surface snow (Aoki et al., 2014). Furthermore, earlier studies have found that snow impurities tend to concentrate at the surface during melting (Doherty et al., 2013; Ming et al., 2016; Qu et al., 2014; Xu et al., 2012). The present study also demonstrated that M_{BC} tends to be low for fresh snow and high for aged surface ice. In addition, the M_{BC} of surface water was lower than that of surface ice. These results suggest that most BC particles were retained in the ice rather than flowing out with the water.

3.1.2 BC, mineral dust, and organic matter in surface ice for altitudes, 2024

Figure 4 portrays box plots of the mass concentrations of BC, mineral dust, and organic matter in water (respectively, M_{BC}, M_{Dust}, and M_{OM}) for surface ice samples collected in 2024. Surface ice conditions were aged snow ice for ACC place, and surface granular ice for stakes 5r, 4c, 3c, and 2c. The M_{BC}, M_{Dust}, and M_{OM} of surface granular ice in ablation (st5r, 4c, 3c, and 2c) vary widely, respectively ranging between 8–600 ng g^{-1}, 0.9–40 mg g^{-1}, and 3–1483 µg g^{-1}. However, those values for all stakes were higher for dark ice, which mainly covered the area, than for white ice, a minor area. As in the 2023 trend, the M_{BC} values of surface ice for dark ice and all samples tended to be highest at st5r (134–601 ng g^{-1}); they decreased by one order with lower altitudes (8–96 ng g^{-1} at st2c). Although the OM mass concentration also shows a weak downward trend with lower altitude for dark ice and all samples, no such downward trend was found for mineral dust.

The amount of organic matter can be influenced by biological activity on ice. Mineral dust in the ablation area can also be supplied from rocks in the glacier and the bottom of the glacier. Because there are no specific local factors for increase and decrease in BC, the amount is affected most strongly by wet deposition, enrichment and dilution in a glacier, and outflow. Several reports have described trends of increasing impurity concentrations with low elevation in the accumulation areas of glaciers in Central Asia (Li et al., 2017, 2018; Zhang et al., 2020), which can be attributed to snow aging processes, including sublimation and evaporation, as well as snowmelt amplification. The BC mass concentration in surface ice found from our study was also the highest at the ablation area near the accumulation area (st5r). However, they decreased with lower elevation among stakes 5r, 4c, 3c, and 2c, which is the inverse of trends reported for accumulation areas in earlier studies. In the ablation area, water is lost from the surface mainly by out flow of the passing water channel rather than by sublimation or evaporation. The flowing water can run off some BC. Therefore, enrichment effects of BC with snowmelt might decrease in the downstream region of the ablation area.

3.1.3 BC size distributions

Figure 5 presents normalized mass–size distributions of BC in the samples, 2023 and 2024, used in Figs. 2 and 3. Averages, minimum and maximum values of M_{BC}, and lognormal fitting results are presented in Table 2 for 2023 and in Table 3 for 2024. Most of the size distributions have peak diameters of 200–400 nm. From several samples, BC larger than 1 µm were also detected. Some earlier studies using a nebulizer and a wide-range SP2 system (Mori et al., 2019, 2021; Schwarz et al., 2013) have revealed the presence of BC particles larger than 1 µm in rain and snow samples. The results suggest that measuring widely various BC sizes is important for accurately quantifying BC mass concentrations and for understanding their effects on snow/ice albedo.

The size distribution for snow and surface snow samples in 2023 often had sharp shapes around the peak. The modal geometric standard deviations, σ_{gm} are, respectively, 1.76–1.81 and 1.82–2.36. The σ_{gm} values are approximately equal to values reported for atmospheric aerosols (1.63–1.76 over the north polar region, as measured by aircraft; Ohata et al., 2021), surface snow (1.66–2.21 in Arctic regions; Mori et al., 2019), and snowfall (1.5–2.1 at Ny-Ålesund; Mori et al., 2021). However, the mass–size distributions for surface ice tended to have broad size distributions (σ_{gm} is 2.06–2.43). The distributions of water samples were also broad for most samples (σ_{gm} is 1.77–2.36). For surface snow samples in 2024, including aged snow ice at ACC, most of the distributions were also wide (average of σ_{gm} for dark ice at each stake is 2.41–3.00). Although M_{BC} had trends depending on altitude, as explained in Sect. 3.1.2, no clear trend was found for the shape of size distributions.

The reason for the broader BC size distributions in ice and water samples that experienced melting and refreezing, compared to those in snow samples, remains unclear. Possible reasons include size-dependent outflows of meltwater from ice and coagulation of BC particles during melting. For outflow with melted water, if smaller (or larger) BC is more easily scavenged out as ice melts and flows out, then differences in the BC size distribution can be expected between surface ice and surface water. However, the BC size distributions of surface water and surface ice on the same day were similar (Fig. 5a, right column); the dependence on BC size in the flow-out was unclear. For coagulation, because the BC concentration was higher in the surface ice samples, we infer that BC particles can contact and coagulate more easily in snow/ice meltwater around surface ice. Although sample vials were sonicated before BC measurement, strongly connected BCs might remain.

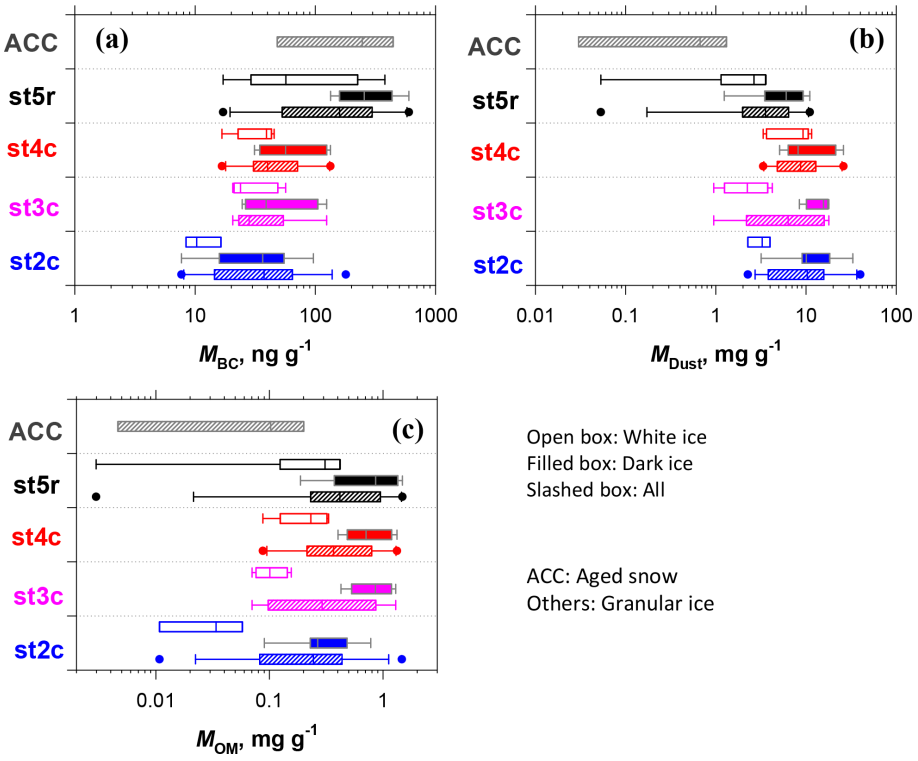

Figure 4. Box plots of the mass concentration of BC, mineral dust, and organic matter in water (M_{BC}, M_{Dust}, and M_{OM}) for surface ice samples collected during 22 July–2 August in 2024. The left boundary of the box shows the 25th percentile. The line within the box represents the median. The right boundary of the box stands for the 75th percentile. The whiskers left and right of the box respectively show the 90th and 10th percentiles.

Table 2. Average [Minimum–Maximum] values of BC mass concentrations and parameters of mass–size distribution for samples collected in 2023.

	M_{BC} [ng g^{-1}]			MAD[a] [nm]	D_{gm}^{b} [nm]	σ_{gm}^{b}
	70–850 nm	850–3000 nm	total			
Rain	2.8 [1.5–4]	0.8 [0.2–2]	3.6 [1.7–6.1]	190 [156–228]	317 [194–443]	2.11 [1.62–2.41]
Snow	2.3 [1.8–2.9]	0.3 [0.3–0.3]	2.6 [2.1–3.2]	185 [180–191]	254 [249–260]	1.78 [1.76–1.81]
Surface snow	8.3 [4.3–18.3]	1.6 [0.3–4.4]	9.9 [5.4–22.7]	176 [161–190]	251 [215–270]	1.99 [1.82–2.36]
Surface ice	223 [38.7–499]	28.9 [3.2–55.8]	252 [42–555]	169 [164–172]	252 [229–270]	2.21 [2.06–2.43]
Surface water	4.8 [1.7–9.3]	0.7 [0–1.6]	5.5 [1.8–10.9]	171 [152–191]	253 [201–300]	2.12 [1.77–2.36]

[a] Mass averaged diameter (MAD) was estimated as $(6M_{BC}/\pi\rho_{BC}N_{BC})^{1/3}$. ρ_{BC} and N_{BC} respectively represent, the BC mass density (= 1.8 g cm^{-3}) and number concentration of BC. [b] Modal geometric mean diameter (D_{gm}) and the modal geometric standard deviation (σ_{gm}) by mono-modal lognormal fitting of mass–size distribution for BC less than 1000 nm.

3.1.4 Water insoluble particles of submicrometer size

Figure 6 shows STEM images and elemental maps of water-insoluble particles collected at the smallest particle stage for a snow sample and for two surface ice samples. Aggregations of small (less than 50 nm diameter) monomer globules, which are characteristic of soot particles (Janzen, 1980; Murr and Soto, 2005; Pósfai et al., 2004; Sachdeva and Attri, 2008; Samson et al., 1987; Ueda et al., 2022), were found in a snow sample (Fig. 6a). However, we were unable to find such bare soot particles from surface ice samples because many other particles were dominant for the surface ice samples. For example, insoluble particles in surface ice samples at st5r were mainly aggregated particles, composed primarily of C, O, and Si (Fig. 6b). Although their shape is similar to that of soot, the individual spherules in the aggregation had larger diameter (> 100 nm) than soot monomers and were O-rich, indicating that they were composed mainly of organics and silicates rather than soot. In surface ice at st2c, most of the insoluble particles were angular particles composed mainly of Si, O, and Al, regarded as aluminosilicates (Fig. 6c). The

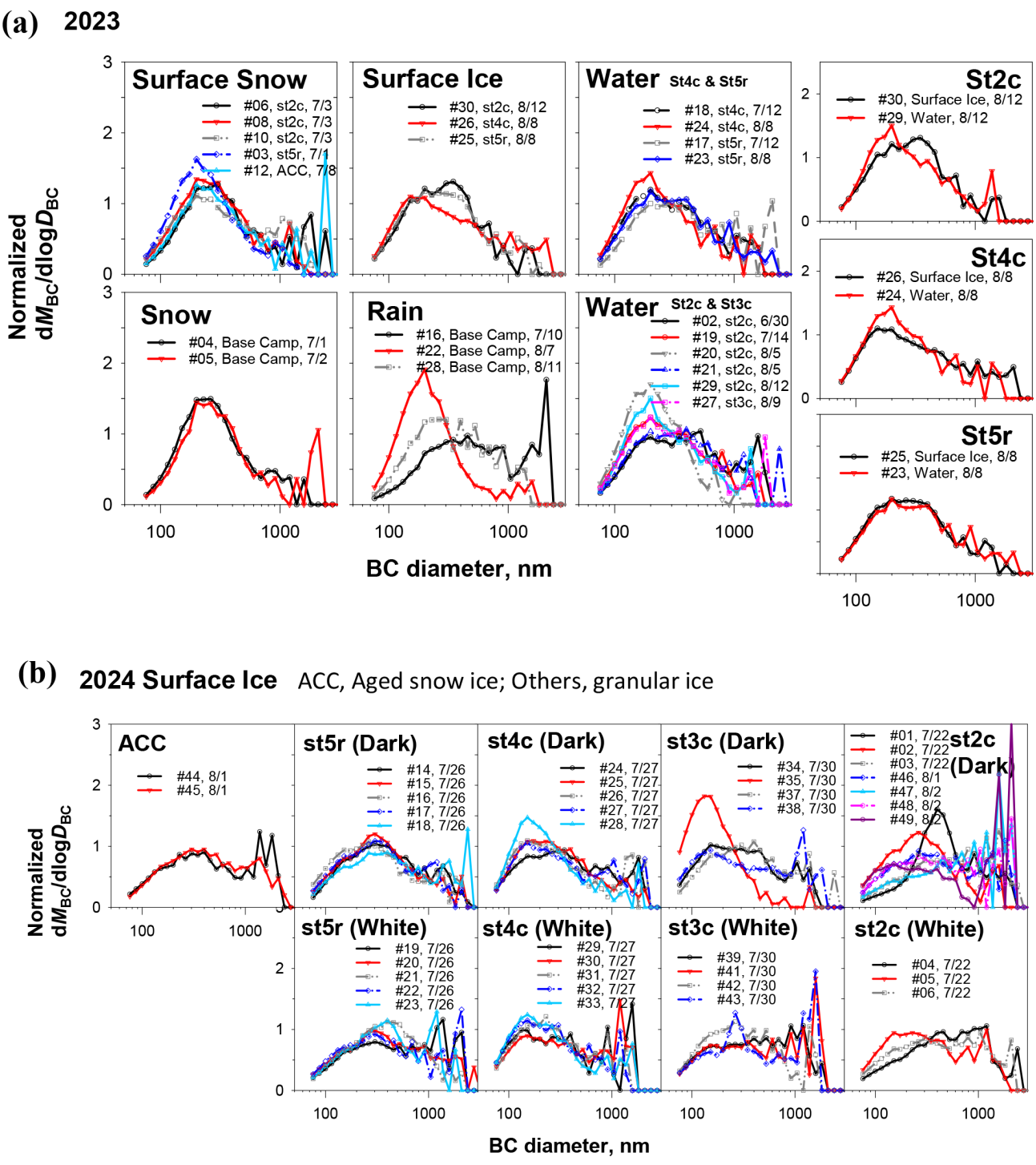

Figure 5. Normalized mass–size distributions of BC in the samples: 2023 and 2024.

minor mass concentration of BC compared to those of mineral dust and organic matter corresponds to results found for mass concentrations, as presented in Sect. 3.1.2.

Soot, an insoluble core commonly found in submicrometer atmospheric aerosols, is visible in the atmosphere over East and South Asia in bare soot and soot with a coating of sulfates and organic matter (Chen et al., 2023; Li et al., 2016, 2024; Ohata et al., 2018; Pang et al., 2023; Ueda et al., 2011a, b, 2016). In our earlier studies of Asian aged pollution and remote atmospheric aerosol conducted using water dialysis (Ueda et al., 2011a, b, 2018, 2023), no case was found for submicrometer insoluble aerosol samples in which

Table 3. Average [Minimum–Maximum] values of BC mass concentrations and parameters of mass–size distribution for samples collected in 2024.

		M_{BC} [ng g^{-1}]			MAD[a] [nm]	D^{b}_{gm} [nm]	σ^{b}_{gm}
		70–850 nm	850–3000 nm	total			
ACC		179 [33–325]	66 [15–118]	245 [48–443]	190 [188–192]	333 [316–350]	2.50 [2.48–2.53]
St5r	dark	229 [109–476]	59 [24–124]	288 [133–600]	176 [161–187]	294 [238–326]	2.41 [2.23–2.58]
	white	91 [11–317]	22 [5–61]	113 [17–379]	185 [178–192]	351 [306–388]	2.72 [2.28–3.21]
St4c	dark	61 [28–103]	13 [2–29]	74 [31–133]	160 [150–169]	224 [182–284]	2.4 [1.92–2.96]
	white	28 [13–36]	5 [3–11]	34 [16–45]	154 [148–161]	206 [182–234]	2.70 [2.26–3.53]
St3c	dark	47 [23–101]	9 [0–23]	56 [24–124]	154 [124–175]	209 [139–295]	2.82 [1.75–4.26]
	white	23 [13–42]	8 [2–14]	31 [20–56]	174 [165–178]	302 [243–429]	3.00 [2.41–4.55]
St2c	dark	26 [4–60]	12 [1–36]	38 [7–96]	191 [162–229]	324 [194–470]	2.49 [1.6–3.18]
	white	8 [6–11]	3 [2–4]	11 [8–16]	182 [165–200]	349 [251–503]	2.78 [2.61–2.96]

[a] Mass averaged diameter (MAD) was estimated as $(6M_{BC}/\pi\rho_{BC}N_{BC})^{1/3}$. ρ_{BC} and N_{BC} respectively represent, the BC mass density ($= 1.8\,g\,cm^{-3}$) and number concentration of BC. [b] Modal geometric mean diameter (D_{gm}) and the modal geometric standard deviation (σ_{gm}) by mono-modal lognormal fitting of mass–size distribution for BC less than 1000 nm.

soot was so minor relative to organics and dust that it was undetectable. As reference, for this study, after three aerosol samples were collected in 2024 at Base Camp, they were observed using TEM (Figs. S1 and S2 of the Supplement). Soot attached to sulfates was often observed, although almost no core of mineral or organic aggregates was found, even after water dialysis. However, for surface ice, a long time has passed since snow deposition, during which local deposition and impurity-enhancement processes have occurred. Organic and silicate insoluble particles found in the surface ice samples could be attributed to local dust and biological activity on ice, such as broken pieces of coarse particles or sediments formed after post-deposition. Particularly, the almost homogeneous mixing states of aggregation containing C and Si (not external mixing states) at st5r imply that they were sediments formed in samples. Silicate and carbonate can form poor-water-soluble sediments in water, which might cover BC and bond-coagulated BC.

3.2 BC vertical profile

3.2.1 Snow under the lower accumulation area, 2023

Figure 7 presents snow types and BC mass concentrations of the snow pit from the surface to 24 cm depth at the ACC site in 2023. A water-bearing layer and an ice layer were found, respectively, at depths of 17 and 20 cm. The upper layer consisted of melt forms and rounded-grain layers, which probably accumulated after a snowmelt event. The BC mass concentration was lower (3.7 ng g^{-1}) for the sample containing the water-bearing layer than the upper snow layers, but higher (84.0 ng g^{-1}) for the sample containing the ice layer. This structure implies the separation of BC from the upper layer with snowmelt and enrichment at the ice layer.

3.2.2 Core samples at the lower ablation area, 2022

Figure 8 presents a vertical profile of BC, OM, and mineral dust for core samples collected at st2c, 31 August 2022, and at st3c, 1 September 2022. For st2c, a high-concentration layer of BC, dust, and organic matter (respectively, 64 ng g^{-1}, 4.4 mg g^{-1}, and 0.2 mg g^{-1}) was found at depths of 15–20.5 cm. However, those concentrations from just below the layer and below were low (respectively, $<$ 16 ng g^{-1}, $<$ 2.0 mg g^{-1}, and $<$ 0.01 mg g^{-1}). Similar trends were found for st3c: a high concentration layer at depths of 0–15 cm and lower concentrations below this layer. The vertical profiles suggest that events of high impure-particle deposition, equivalent to the BC concentration of the surface ice, were rare in this observation site. Therefore, the high concentration of BC near the surface could be attributed mainly to melting processes at the snow and ice surface, rather than to the wet and dry deposition of atmospheric particles.

3.2.3 Surface wet snow and the underlying weathering granular ice

Weathering granular ice layers with high concentrations of BC were located within 8 cm below the surface (Tables S4 and S5). However, the layers were sometimes covered by wet snow. Figure 9 portrays the number–size and mass–size distributions of BC for snow/granular ice samples collected at st2c, 3 July 2023. The BC concentrations of the granular ice for most BC sizes were higher than those of the upper wet snow layer, which was 2–3 cm thick. Both the BC mass size distribution of upper wet snow and lower granular ice had a similar broad shape.

To understand such surface structure and BC enrichment with snow melting, we conducted a simple test for snow

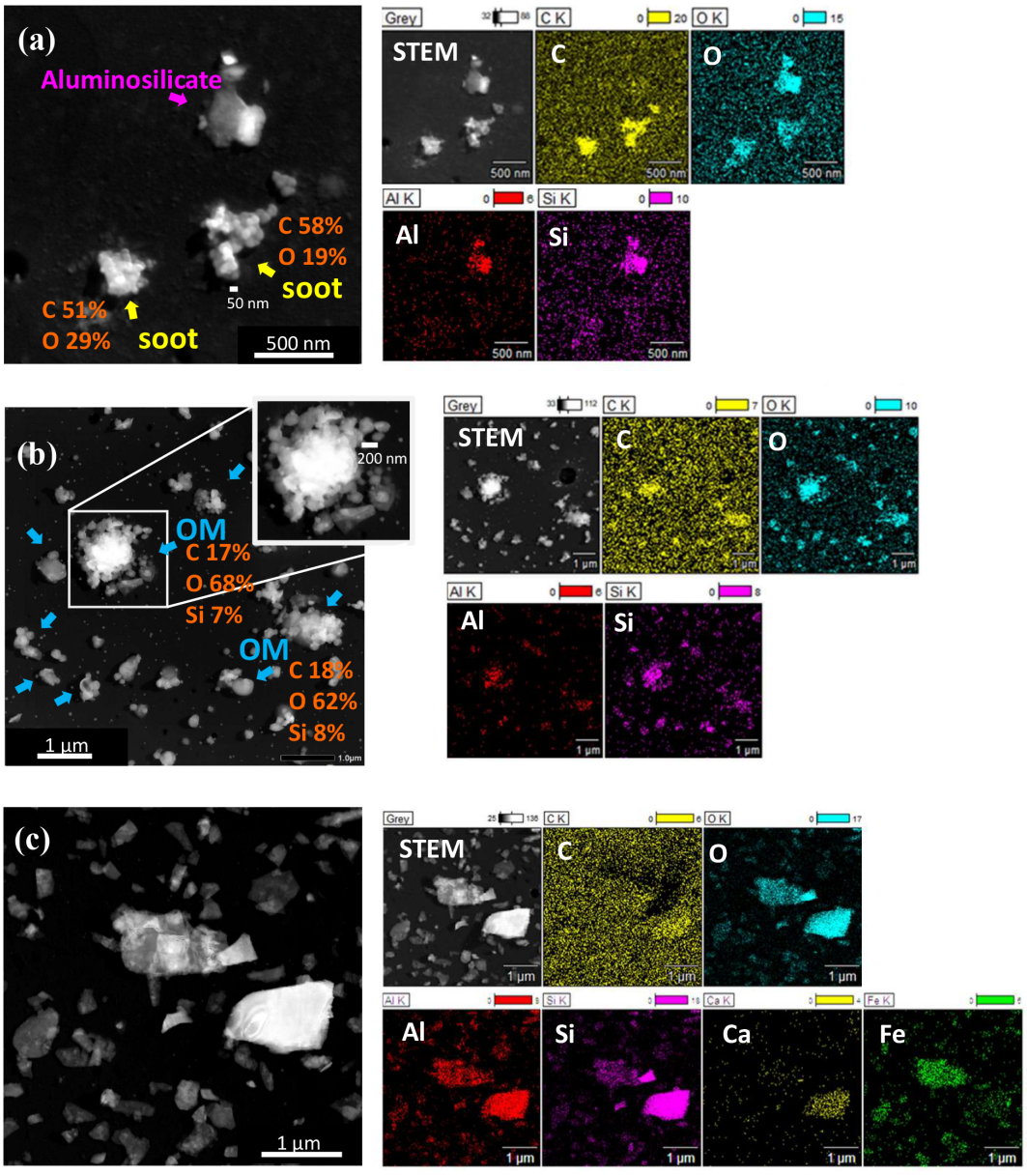

Figure 6. STEM images and elemental maps of water-insoluble particles collected at the smallest particle stage: **(a)** soot and aluminosilicate in a snow sample at base camp (23BC#04); **(b)** fine OM particles in surface ice samples at st5r (23BC#25), and fine aluminosilicate particles in surface ice sample at st2c (23BC#30).

melting using a snow block in st2c 2024. After the original snow in a plastic bag was exposed to the sun for 3.5 h, the melted water and residual snow were collected separately. Detailed results are presented in Fig. S3. The BC concentration of the melted water (15.4 ng g^{-1}) was higher than that of the residual snow (4.5 ng g^{-1}). Light absorption by BC particles can explain this result: snow around BC particles preferentially melted and fell below, consequently being stored at the bottom of the plastic bag in this experiment. Over the glacier surface at the ablation area, the down-flowing water can partly flow out to water channels, be retained partly in the ice, and be refrozen. The high concentration of BC in granular ice might therefore be formed through the retention and refreezing of flowed-down, BC-enriched water.

3.3 Enrichment and outflow of BC over the ablation area

3.3.1 Inference of the BC enrichment process

As described in Sect. 3.1.1 and 3.2.1, the BC concentration in surface ice that had experienced melting and refreezing (i.e. weathering granular ice and ice layers) was significantly higher than in either snow or wet snow. This higher concen-

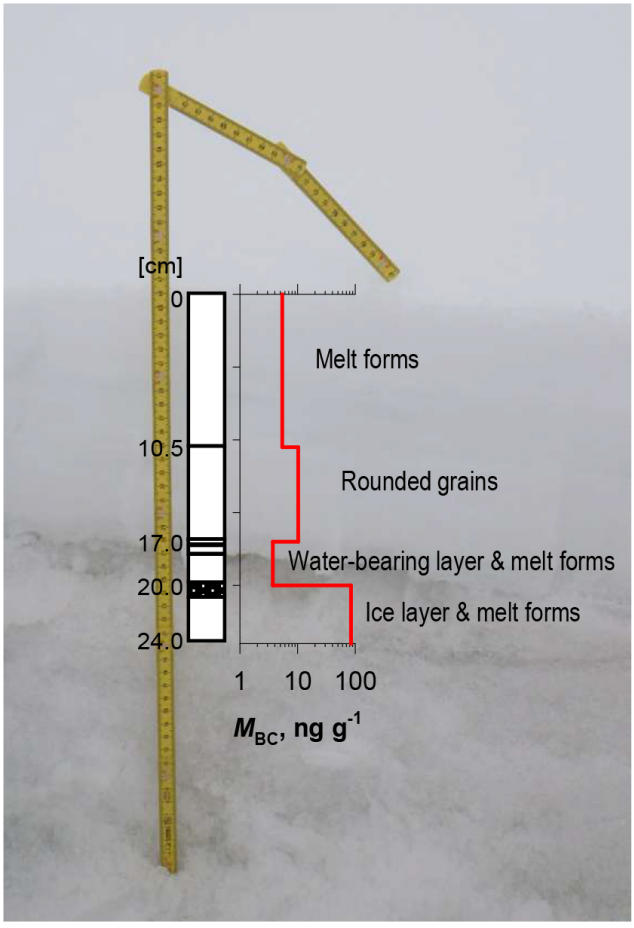

Figure 7. Vertical profile of BC and snow types for snow pit at the ACC site, 2023.

tration suggests that BC is enriched by the melting of snow and ice. As shown in Sect. 3.1.2, the BC concentration in surface ice was highest in St5R (the upstream part of the ablation area). It decreased towards the downstream area. This result suggests that the balance between retained and lost BC differs for different elevations.

Several reports have described enrichment with melting (Doherty et al., 2013; Ming et al., 2016; Qu et al., 2014; Xu et al., 2012), but the mechanism remains unclear. As explained in Sect. 3.2.2, light-absorbing particles absorb shortwave radiation and consequently sink preferentially as they melt the surrounding snow. However, layers with a high BC concentration were near the surface. The BC concentration of surface flowing water was one or two orders of magnitude lower than the surrounding surface ice. This low concentration suggests that many light-absorbing particles are trapped in the ice below the surface and that water with a low BC concentration is preferentially flowing out. Based on inference from earlier studies and this observation, insoluble particles remain for several possible reasons. (1) Light-absorbing particles that settle preferentially refreeze first in the lower layer, where the ice temperature is low. This refreezing creates a hard ice plate that fixes particles in place. (2) When melting, the granular ice in the lower layer acts as a filter, allowing only water to flow out through the channels. (3) At night, the concentrated layer of BC in the lower layer freezes. However, the diluted surface layer of BC melts because of heat conduction from the atmosphere, flowing out and leaving behind the solid lower layer. Several factors can influence the ability of ice to retain BC: the structure and density of the weathering granular ice, the melting rate and frequency, as well as the elevation and temperature of the atmosphere, surface, and layers.

3.3.2 Remaining BC mass in surface granular ice

As shown in Fig. 8, the concentration of impurities in the surface granular ice was markedly higher than that below the surface. Therefore, surface granular ice is regarded as rich in impurities. The surface granular ice usually had 1–8 cm thickness (Tables S3 and S4). Figure 10 shows the weight of surface granular ice per unit area for the dark ice covering most of the surface for st5r, 4c, 3c, and 2c in 2023 and 2024, as well as the total and size-segregated (70–850 and 850–3000 nm) BC mass in the surface granular ice in 2024. The masses of surface granular ice (m_{WC}) and BC mass in the surface granular ice (m_{surfBC}) were, respectively, 0.2–4.4 g cm^{-2} and 5.7–896 ng cm^{-2}.

Annual BC deposition fluxes calculated using a global model CAM-ATRAS are listed in Table S5 in the Supplement. Based on calculations made using a global model (CAM-ATRAS), annual deposition in this region over the past 10 years was estimated as 896–1494 ng cm^{-2} yr^{-1}. The recharge rate of Potanin, calculated using a mass balance model based on the mass balance obtained from the stake observations (2003–2018), is 621 mm yr^{-1} in terms of precipitation (Khalzan et al., 2022). By multiplying this quantity by the average BC concentration of snow samples collected in 2023, which is 2.7 ng g^{-1}, the roughly calculated annual flux is 1675 ng cm^{-2} yr^{-1}, a value similar to the BC deposition predicted by the model, thereby supporting the validity of the model results. In addition, based on measurements of the stakes' surface height, the yearly snow/ice loss (A_w, water ablation weight) at st5r, 4c, 3c, and 2c are, respectively, 246 g cm^{-2} (= cm water equivalent), 274, 264, and 325 g cm^{-2} per year on a three-year average. Considering that the BC mass concentration under the BC-enrichment layer ($M_{underBC}$) is 4.4 ng g^{-1} on average in ice cores from 15 cm depth to 3 m depth, the BC weight in ablated snow under the surface (A_{BC}) is estimated roughly as 1080–1429 ng cm^{-2} as $M_{underBC} \times A_w$. Both the annual deposition of BC and A_{BC} were higher than, but of the same order as, the highest m_{surfBC} (896 ng cm^{-2}) in st5r.

Although m_{WC} changed less with elevation, the m_{surfBC} tended to be exponentially smaller at lower altitudes. For size-segregated BC, the exponential index slope was slightly

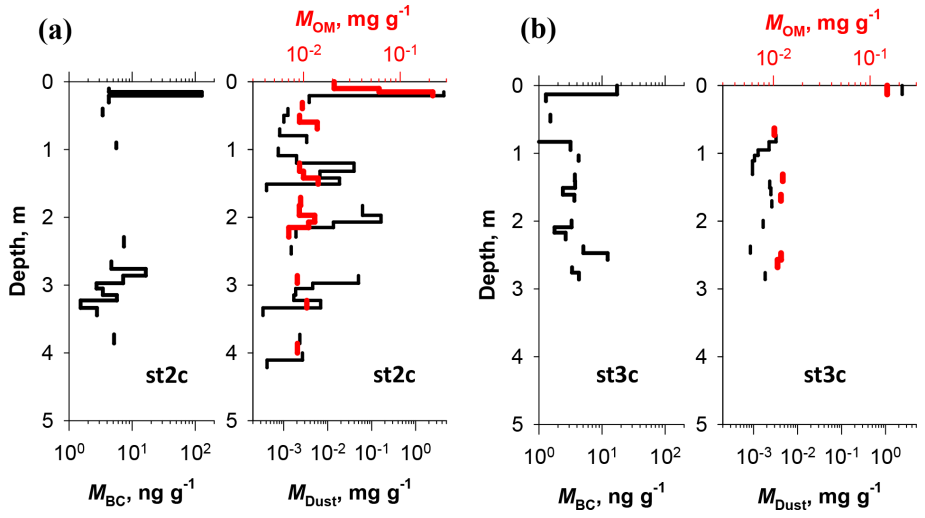

Figure 8. Vertical profile of BC, organic matter, and mineral dust for ice core samples drilled at st2c on 31 August 2022 **(a)** and at st3c on 1 September 2022 **(b)**. Cases for which no data were obtained because of storage vial cracking are blanked.

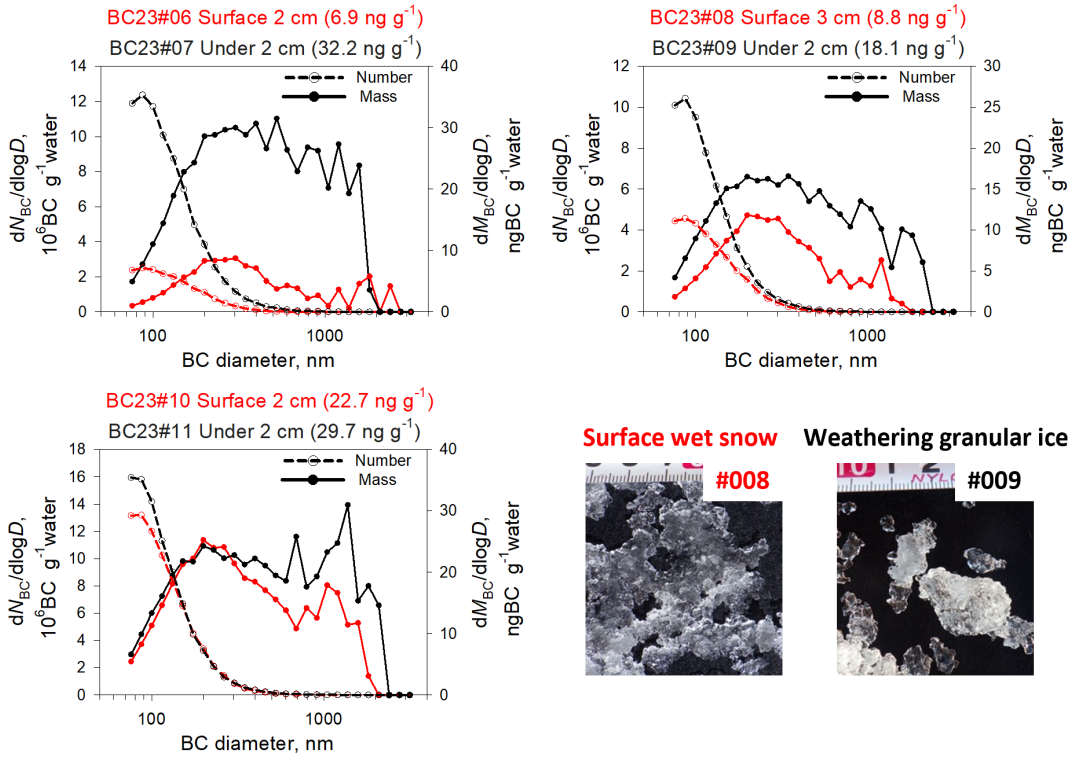

Figure 9. Number–size and mass–size distribution of BC for surface wet snow and the underlying weathering granular ice samples collected at st2c, 3 July 2023.

larger for particles smaller than 850 nm. However, the difference was not great. These results suggest that retention of BC particles in the surface granular ice decreases concomitantly with decreasing altitude, irrespective of particle size.

3.3.3 Estimation of BC remaining fraction on surface ice with meltwater outflow

As explained in Sect. 3.3.2, the values of BC in surface granular ice were smaller than the yearly deposition of BC and the amount of BC in ablated water, but they might be comparable. As discussed in Sect. 3.3.1, various processes related to

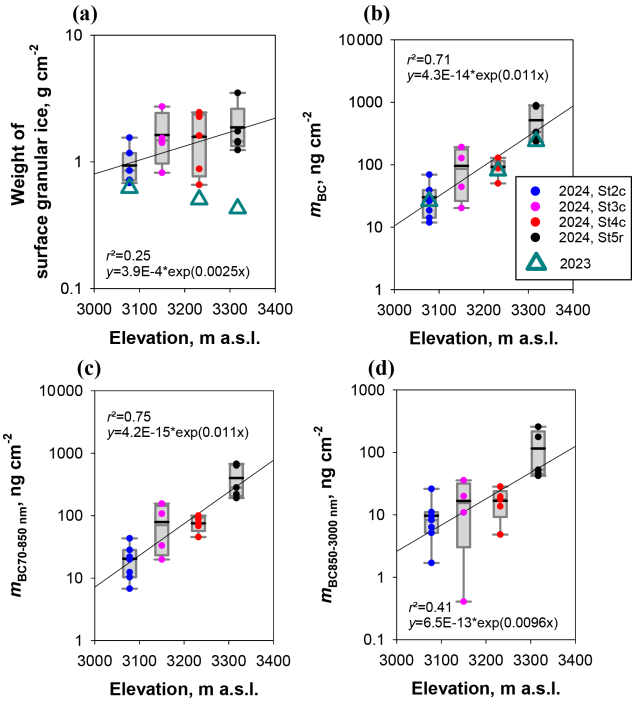

Figure 10. Relation of elevations with weight of surface granular ice per unit area **(a)** and total BC **(b)** in 2023 and 2024, and size-segregated BC mass **(c, d)** in surface granular ice for st5r, 4c, 3c, and 2c in 2024. Dark ice samples, which covered most of the surface, were used, whereas white ice was excluded because of its minor area.

altitude and temperature can affect the concentration of BC particles in surface ice. For this study, we calculate the surface granular ice's ability to retain BC particles at each stake in the ablation region, based on observed BC concentrations and snow ablation rates. We estimated the surface remaining fraction of BC to BC contained in lost water over a year (R: annual remaining fraction) as an indicator of the surface granular ice's ability. The mass of BC remaining on the ablation surface in a given year ($m_{\mathrm{surfBC}}(t)$) can be expressed in terms of the prior year's mass ($m_{\mathrm{surfBC}}(t-1)$), as shown below.

$$m_{\mathrm{surfBC}}(t) = (m_{\mathrm{surfBC}}(t-1) + F_{\mathrm{BC}} + A_{\mathrm{BC}}) \times R$$
$$A_{\mathrm{BC}} = M_{\mathrm{underBC}} \times A_{\mathrm{w}}$$
$$0 \le R \le 1 \quad (1)$$

Therein, F_{BC} represents the deposition flux of BC from air for a year. In addition, as F_{BC}, 1228 ng cm^{-2} yr^{-1} was used. It was the averaged values of 2021–2023, as estimated using CAM-ATRAS. Strictly speaking, F_{BC} can differ spatially when precipitation is heterogeneous. However, based on observation results obtained from an earlier study (Khalzan et al., 2022), precipitation at the altitudes of st2c–st5r was similar (about a 11 % difference); F_{BC} can also be inferred as showing less change across this area. Although M_{underBC} is also strictly variable, an averaged value was used (= 4.4 ng g^{-1}). Equation (1) is expanded as presented below.

$$\begin{aligned} m_{\mathrm{surfBC}}(t) &= (m_{\mathrm{surfBC}}(t=0)) \times R^t + (F_{\mathrm{BC}} + A_{\mathrm{BC}}) \\ &\quad \times (R + R^2 + R^3 + \ldots + R^t) \\ &= (m_{\mathrm{surfBC}}(t=0)) \times R^t + (F_{\mathrm{BC}} + A_{\mathrm{BC}}) \\ &\quad \times \frac{R(1-R^t)}{(1-R)} \end{aligned} \quad (2)$$

The value of $m_{\mathrm{surfBC}}(t)$ converges to the following.

$$m_{\mathrm{surfBC}} \simeq (F_{\mathrm{BC}} + A_{\mathrm{BC}}) \times \frac{R}{(1-R)} \quad (3)$$

This status of $m_{\mathrm{surfBC}}(t)$ and $m_{\mathrm{surfBC}}(t-1)$ is mostly the same, independent of t. The value of $m_{\mathrm{surfBC}}(t)$ converges more quickly if R is smaller. As presented in Fig. 10, the m_{surfBC} values of 2024 were those of 2023 for st2c, 4c, and 5r, which can be regarded as $m_{\mathrm{surfBC}}(t) \simeq m_{\mathrm{surfBC}}(t-1)$, an almost converged state, at these sites. Therefore, R is developed using Eq. (3) as the expression presented below.

$$R \simeq \frac{m_{\mathrm{surfBC}}}{m_{\mathrm{surfBC}} + F_{\mathrm{BC}} + A_{\mathrm{BC}}} \quad (4)$$

Strictly speaking, R can depend on t because they differ according to elevation. However, the glacier flow velocities at st5r, 4c, 3c and 2c are, respectively, 59, 27, 1.5, and 1.0 m yr^{-1} (Table 1). The horizontal distances between st5r and 4c, 4c and 3c, and 3c and 2c are, respectively, 1.4, 1.4, and 1.3 km. Even with the rapid upstream flow from st5r to st4c, it takes longer than two decades. The movement and elevation changes of stakes can be regarded as less within a year. Here, we considered R change less on a few-year scale in this case. We therefore used Eq. (4). In this case, $F_{\mathrm{BC}} + A_{\mathrm{BC}}$ corresponds to BC, which runs off in a year per unit of the area.

The estimated R values and the values used for estimation are presented in Table 4. The average values of R are 0.17, 0.036, 0.038, and 0.011, respectively, for st5r, 4c, 3c, and 2c, suggesting a decreasing trend in the ability of snow to retain BC particles downstream. Despite an increase in A_{w} of only approximately 30 % from St5r to St2c, the calculated R value for St2c was one order of magnitude lower than that for St5r. By contrast, the R values were almost identical at St4 and St3, despite their different altitudes, because both the A_{w} and m_{surfBC} values were almost identical at these two locations. The m_{surfBC}, residual BC in surface granular ice, might also depend on the A_{w}, relating to factors such as the structure of granular ice and the water flow pressure. The rate of water loss might have a stronger effect on the particle retention capacity of granular ice than elevation. As explained in Sect. 3.3.1, the enhancement of BC with the snow/ice melting process is related to multiple processes. An increase in A_{w} with low elevation can affect multiple factors, including the reach length to a water channel and the structure of

Table 4. BC mass in the surface granular ice (m_{surfBC}) in 2024, water ablation weight (A_{w}), BC in annual ablated snow (A_{BC}), and the annual remaining fraction of BC (R) for each stake.

	m_{surfBC} [ng BC cm^{-2}] Avg. [Min.–Max.]	A_{w} [g water yr^{-1}] 3 year average	A^{*}_{BC} [ng BC cm^{-2} year^{-1}]	$R*$ Avg. [Min.–Max.]
St5r	517 [234–896]	246 ± 25	1080	0.17 [0.09–0.28]
St4c	92 [50–129]	274 ± 38	1206	0.036 [0.02–0.05]
St3c	96 [20–192]	264 ± 27	1162	0.038 [0.008–0.074]
St2c	30 [12–70]	325 ± 11	1429	0.011 [0.004–0.026]

* Values estimated assuming $M_{\mathrm{underBC}} = 4.4\,\mathrm{ng\,g^{-1}}$ and $F_{\mathrm{BC}} = 1228\,\mathrm{ng\,cm^{-2}\,yr^{-1}}$.

the weathering granular ice. Such an increase might consequently decrease the particle filtered efficiency of granular ice.

Doherty et al. (2013), based on surface and subsurface snow BC concentrations observed at Barrow, estimated the scavenging fraction for snow melting as 10 %–30 % (i.e. a remaining fraction of 0.7–0.9). For this study, the R value for the accumulated lost water over the year is lower than the remaining fraction (0.7–0.9) because it represents the remaining fraction to a more extended period (one year), incorporating the effects of multiple factors including the melting event frequency and the surface ice structure, as well as the period during which the granular ice is covered by snow accumulation in winter. Although the remaining fractions at different locations differed considerably on an annual scale, assuming roughly three months of snowmelt, the surface remaining fraction of BC for a day (R_{day}) can be estimated as $R^{1/(90\,\mathrm{d})}$: 0.98, 0.96, 0.96, and 0.95, respectively, for st5r, 4c, 3c, and 2c, which indicates that most BC is retained in the surface ice on a daily basis. That finding corresponds to the observation that the BC concentration in surface water is nearly two orders of magnitude lower than that in surface ice.

4 Summary and conclusions

We investigated BC mass concentrations (M_{BC}) of snow and ice samples acquired from the ablation area of Potanin Glacier in Mongolia during the summers of 2022, 2023, and 2024. Of the various snow and ice types, surface snow had slightly higher M_{BC} values (5–22 ng g^{-1}) than precipitation (2–6 ng g^{-1}), although these were much lower than those of surface ice (42–555 ng g^{-1}). Additionally, the M_{BC} values for surface water (2–11 ng g^{-1}) originating from the melting of surface ice were low. Vertical profiles of BC showed a high concentration of BC in the surface layer and a low concentration below it. These findings suggest that the surface ice layer was rich in impurities, probably because of the presence of particles in the weathering granular ice and because of the flow of particle-free water out of the ablation area. The BC mass–size distribution of surface snow, ice, and water typically peaks in the range of 200–400 nm. Moreover, it has a broader shape than that of fresh snow and rain. These results, together with the coexistence of dust and organic matter as observed using TEM, suggest coagulation with enrichment of impurity particles.

The M_{BC} values over the ablation area in 2024 exhibited a clear decreasing trend with elevation, with the highest (134–601 ng g^{-1}) at the st5r (3317 m) site and one order of magnitude lower (8–96 ng g^{-1}) at the st2c (3078 m) site. In the ablation area, water is lost from the surface mainly by outflow of the passing water channel rather than by sublimation and evaporation. The enrichment effect of BC with snowmelt might decrease in the downstream region of the ablation area. By contrast, for mineral dust, no change in the order of mass concentration with altitude was observed. However, vertical profiles indicated an enrichment trend of organic matter, dust and BC at the glacier surface. Factors affecting the increase and decrease in BC among impurities are limited primarily to deposition and the balance of dilution and enrichment within glaciers. This characteristic of limitation differs from that of organic matter, which can be affected by biological activity in the ice, and mineral dust, which can originate from the glacier itself and its base. For the case in which the BC concentration is regarded as less affected by local emissions, as in this study, the BC concentration can be an indicator of the enrichment process which occurs with melting.

Considering BC vertical profiles and simple experiments involving a snow block in a plastic bag, light-absorbing particles absorb shortwave radiation and consequently sink preferentially as they melt the surrounding snow. However, BC-enriched layers were observed near the surface, suggesting that light-absorbing particles were trapped in the surface granular ice and that they rarely flowed out. Various factors can influence the ability of the granular ice to retain BC, including the weathering granular ice structure, melting conditions, and the atmosphere and ice temperatures. For this study, the residual surface rate of BC to BC contained in lost water over a year (R: the annual remaining fraction) in the ablation region was calculated using yearly snow/ice loss (A_{w}: the water ablation weight). The average R values were 0.17 at st5r, $A_{\mathrm{w}} = 246\,\mathrm{g\,cm^{-2}}$, and 0.011 at st2c, $A_{\mathrm{w}} = 325\,\mathrm{g\,cm^{-2}}$. These findings suggest that the ability to retain BC particles is greater where there is less snow/ice ab-

lation and suggest that the retention ability tends to decrease downstream.

For this study, we estimated the enriched BC concentration through glacier melting and evaluated the ability of surface granular ice to retain BC residue in the ablation area during summer. Unlike the accumulation area, where surface snow is converted into fresh snow, the surface ice in the ablation area consisted of melted and refrozen snow that had migrated from the lower layer. Consequently, enriched BC particles on the ablation area surface contain recently deposited BC and comparable quantities of BC that have accumulated and migrated during decades or centuries. It is noteworthy that BC deposition from the atmosphere, including that from human activities, can influence current and future glacier melting.

Data availability. Observation data for BC, dust, and OM and simulation results by CAM-ATRAS in this study are publicly available through the Supplement. Satellite data were obtained from Data Workspace (https://dataspace.copernicus.eu/analyse/data-workspace, last access: 23 November 2023). Other data will be provided upon request.

Supplement. The supplement related to this article is available online at https://doi.org/10.5194/acp-26-3167-2026-supplement.

Author contributions. AS designed the study. SU wrote the paper. AS, PK, and SM contributed to observations at Potanin glacier. KK calculated the glacier flow velocity. SU, SO and AS analyzed samples. HM conducted numerical model simulations using CAM–ATRAS.

Competing interests. The contact author has declared that none of the authors has any competing interests.

Disclaimer. Publisher's note: Copernicus Publications remains neutral with regard to jurisdictional claims made in the text, published maps, institutional affiliations, or any other geographical representation in this paper. The authors bear the ultimate responsibility for providing appropriate place names. Views expressed in the text are those of the authors and do not necessarily reflect the views of the publisher.

Acknowledgements. We acknowledge Azusa Kishi of Nagoya University for BC analysis. We are indebted to Michihiro Mochida and Kazuo Osada of Nagoya University for their support of the experimentation environment. We also extend our gratitude for technical support from the High Voltage Electron Microscope Laboratory of Nagoya University.

Financial support. This study was supported by Ministry of Education, Culture, Sports, Science and Technology of Japan and the Japan Society for the Promotion of Science (MEXT/JSPS) KAKENHI grant nos. 20H00196, 22K18023, 22K18024, 25H00507, 22H03722, 23H00515, 23H00523, 23K18519, 23K24976, and 24H02225, the MEXT Arctic Challenge for Sustainability II (ArCS II; JPMXD1420318865) and phase 3 (ArCS-3; JPMXD1720251001) projects, and by the Environment Research and Technology Development Fund 2–2301 (JPMEERF20232001) of the Environmental Restoration and Conservation Agency, by National Institute of Polar Research (NIPR) through Special Collaboration Project no. B25-02, and by financial support from the Nagoya University Asian Satellite Campuses Institute (ASCI) Second Stage Project. This work was achieved partly through the use of SQUID at the D3 Center, Osaka University.

Review statement. This paper was edited by Manabu Shiraiwa and reviewed by three anonymous referees.

References

Aoki, T., Matoba, S., Yamaguchi, S., Tanikawa, T., Niwano, M., Kuchiki, K., Adachi, K., Uetake, J., Motoyama, H., and Hori, M.: Light-absorbing snow impurity concentrations measured on Northwest Greenland ice sheet in 2011 and 2012, Bull. Glaciol. Res., 32, 21–31, https://doi.org/10.5331/bgr.32.21, 2014.

Bisiaux, M. M., Edwards, R., McConnell, J. R., Albert, M. R., Anschütz, H., Neumann, T. A., Isaksson, E., and Penner, J. E.: Variability of black carbon deposition to the East Antarctic Plateau, 1800–2000 AD, Atmos. Chem. Phys., 12, 3799–3808, https://doi.org/10.5194/acp-12-3799-2012, 2012a.

Bisiaux, M. M., Edwards, R., McConnell, J. R., Curran, M. A. J., Van Ommen, T. D., Smith, A. M., Neumann, T. A., Pasteris, D. R., Penner, J. E., and Taylor, K.: Changes in black carbon deposition to Antarctica from two high-resolution ice core records, 1850–2000 AD, Atmos. Chem. Phys., 12, 4107–4115, https://doi.org/10.5194/acp-12-4107-2012, 2012b.

Bond, T. C., Doherty, S. J., Fahey, D. W., Forster, P. M., Berntsen, T., DeAngelo, B. J., Flanner, M. G., Ghan, S., Kärcher, B., Koch, D. Kinne, S., Kondo, Y., Quinn, P. K., Sarofim, M. C., Schultz, M. G., Schulz, M., Venkataraman, C., Zhang, H., Zhang, S., Bellouin, N., Guttikunda, S. K., Hopke, P. K., Jacobson, M. Z., Kaiser, J. W., Klimont, Z., Lohmann, U., Schwarz, J. P., Shindell, D., Storelvmo, T., Warren, S. G., and Zender, C. S.: Bounding the role of black carbon in the climate system: A scientific assessment, J. Geophys. Res.-Atmos., 118, 5380–5552, https://doi.org/10.1002/jgrd.50171, 2013.

Chen, X. Y., Ye, C. X., Wang, Y. Y., Wu, Z. J., Zhu, T., Zhang, F., Ding, X. K., Shi, Z. B., Zheng, Z. H., and Li, W. J.: Quantifying evolution of soot mixing state from transboundary transport of biomass burning emissions, Iscience, 26, https://doi.org/10.1016/j.isci.2023.108125, 2023.

Cuffey, K. M. and Paterson, W. S. B.: The physics of glaciers, 4th edn., Amsterdam, etc., Academic Press. 704 pp., ISBN 978-0-12-3694461-4, 2010.

Dean, W. E.: Determination of carbonate and organic matter in calcareous sediments and sedimentary rocks by loss on ignition;

comparison with other methods, J. Sediment. Res., 44, 242–248, 1974.

Doherty, S. J., Grenfell, T. C., Forsstrom, S., Hegg, D. L., Brandt, R. E., and Warren, S. G.: Observed vertical redistribution of black carbon and other insoluble light-absorbing particles in melting snow, J. Geophys. Res.-Atmos., 118, 5553–5569, https://doi.org/10.1002/jgrd.50235, 2013.

Goto-Azuma, K., Dallmayr, R., Ogawa-Tsukagawa, Y., Moteki, N., Mori, T., Ohata, S., Kondo, Y., Koike, M., Hirabayashi, M., Ogata, J., Kitamura, K., Kawamura, K., Fujita, K., Matoba, S., Nagatsuka, N., Tsushima, A., Fukuda, K., and Aoki, T.: Technical note: High-resolution analyses of concentrations and sizes of refractory black carbon particles deposited in northwestern Greenland over the past 350 years – Part 1: Continuous flow analysis of the SIGMA-D ice core using the wide-range Single-Particle Soot Photometer and a high-efficiency nebulizer, Atmos. Chem. Phys., 24, 12985–13000, https://doi.org/10.5194/acp-24-12985-2024, 2024.

Goto-Azuma, K., Ogawa-Tsukagawa, Y., Fukuda, K., Fujita, K., Hirabayashi, M., Dallmayr, R., Ogata, J., Moteki, N., Mori, T., Ohata, S., Kondo, Y., Koike, M., Matoba, S., Kadota, M., Tsushima, A., Nagatsuka, N., and Aoki, T.: High-resolution analyses of concentrations and sizes of refractory black carbon particles deposited in northwestern Greenland over the past 350 years – Part 2: Seasonal and temporal trends in refractory black carbon originated from fossil fuel combustion and biomass burning, Atmos. Chem. Phys., 25, 657–683, https://doi.org/10.5194/acp-25-657-2025, 2025.

Hansen, J. and Nazarenko, L.: Soot climate forcing via snow and ice albedos, P. Natl. Acad. Sci. USA, 101, 423–428, https://doi.org/10.1073/pnas.2237157100, 2004.

Heid, T. and Kääb, A.: Evaluation of existing image matching methods for deriving glacier surface displacements globally from optical satellite imagery, Remote Sens. Environ., 118, 339–355, https://doi.org/10.1016/j.rse.2011.11.024, 2012.

Hugonnet, R., McNabb, R., Berthier, E., Menounos, B. Nuth, C., Girod, L., Farinotti, D., Huss, M., Dussaillant, I., Brun, F., and Kääb, A.: Accelerated global glacier mass loss in the early twenty-first century, Nature, 592, 726–731, https://doi.org/10.1038/s41586-021-03436-z, 2021.

Hurrell, J. W., Hack, J. J., Shea, D., Caron, J. M., and Rosinski, J.: A new sea surface temperature and sea ice boundary dataset for the Community Atmosphere Model, J. Climate, 21, 5145–5153, https://doi.org/10.1175/2008JCLI2292.1, 2008.

Janzen, J.: Extinction of light by highly nonspherical strongly absorbing colloidal particles: spectrophotometric determination of volume distributions for carbon blacks, Appl. Optics, 19, 2977–2985, https://doi.org/10.1364/AO.19.002977, 1980.

Kaspari, S., Schwikowski, M., Gysel, M., Flanner, M. G., Kang, S., Hou, S., and Mayewski, P. A.: Recent increase in black carbon concentrations from a Mt. Everest ice core spanning 1860–2000 AD, Geophys. Res. Lett., 38, L04703, https://doi.org/10.1029/2010GL046096, 2011.

Kaspari, S., Painter, T. H., Gysel, M., Skiles, S. M., and Schwikowski, M.: Seasonal and elevational variations of black carbon and dust in snow and ice in the Solu-Khumbu, Nepal and estimated radiative forcings, Atmos. Chem. Phys., 14, 8089–8103, https://doi.org/10.5194/acp-14-8089-2014, 2014.

Khalzan, P., Sakai, A., and Fujita, K.: Mass Balance of Four Mongolian Glaciers: In-situ Measurements, Long Term Reconstruction and Sensitivity Analysis, Front. Earth Sci., 9, 785306, https://doi.org/10.3389/feart.2021.785306, 2022.

Khalzan, P., Sadyrov, S., Sakai, A., Tanaka, K., and Fujita, K.: Glacier meltwater contribution to river runoff in Western Mongolia, J. Hydrol., 59, 102375, https://doi.org/10.1016/j.ejrh.2025.102375, 2025.

Konya, K., Yamaguchi, M., Takigawa, M., Miyakawa, T., and O'Neel, S.: Mass concentration and origin of black carbon in spring snow on glaciers in the Alaska Range, Polar Sci., 27, 100572, https://doi.org/10.1016/j.polar.2020.100572, 2021.

Kuchiki, K., Aoki, T., Niwano, M., Matoba, S., Kodama, Y., and Adachi, K.: Elemental carbon, organic carbon, and dust concentrations in snow measured with thermal optical and gravimetric methods: Variations during the 2007–2013 winters at Sapporo, Japan, J. Geophys. Res.-Atmos., 120, 868–882, https://doi.org/10.1002/2014JD022144, 2015.

Li, W., Riemer, N., Xu, L., Wang, Y., Adachi, K., Shi, Z., Zhang, D., Zheng, Z., and Laskin, A.: Microphysical properties of atmospheric soot and organic particles: measurements, modeling, and impacts, npj Clim. Atmos. Sci., 7, 65, https://doi.org/10.1038/s41612-024-00610-8, 2024.

Li, W. J., Shao, L., Zhang, D., Ro, C.-U., Hu, M., Bi, X., Geng, H., Matsuki, A., Niu, H., and Chen, J.: A review of single aerosol particle studies in the atmosphere of East Asia: Morphology, mixing state, source, and heterogeneous reactions, J. Cleaner Prod., 112, 1330–1349, https://doi.org/10.1016/j.jclepro.2015.04.050, 2016.

Li, X., Kang, S., He, X., Qu, B., Tripathee, L., Jing, Z., Paudyal, R., Li, Y., Zhang, Y., Yan, F., Li, G., and Li, C.: Light-absorbing impurities accelerate glacier melt in the central Tibetan Plateau, Sci. Total Environ., 587–588, 482–490, https://doi.org/10.1016/j.scitotenv.2017.02.169, 2017.

Li, X., Kang, S., Zhang, G., Qu, B., Tripathee, L., Paudyal, R., Jing, Z., Zhang, Y., Yan, F., Li, G., Cui, X., Xu, R., Hu, Z., and Li, C.: Light-absorbing impurities in a southern Tibetan Plateau glacier: variations and potential impact on snow albedo and radiative forcing, Atmos. Res., 200, 77–87, https://doi.org/10.1016/j.atmosres.2017.10.002, 2018.

Liu, M. and Matsui, H.: Aerosol radiative forcings induced by substantial changes in anthropogenic emissions in China from 2008 to 2016, Atmos. Chem. Phys., 21, 5965–5982, https://doi.org/10.5194/acp-21-5965-2021, 2021a.

Liu, M. and Matsui, H.: Improved Simulations of Global Black Carbon Distributions by Modifying Wet Scavenging Processes in Convective and Mixed-Phase Clouds, J. Geophys. Res.-Atmos., 126, e2020 JD033890, https://doi.org/10.1029/2020JD033890, 2021b.

Marquetto, L., Kaspari, S., and Simões, J. C.: Mass and number size distributions of rBC in snow and firn samples from Pine Island Glacier, West Antarctica, Earth Space Sci., 7, e2020EA001198, https://doi.org/10.1029/2020EA001198, 2020.

Matsui, H.: Development of a global aerosol model using a two-dimensional sectional method: 1. Model design, J. Adv. Model. Earth Sy., 9, 1921–1947, https://doi.org/10.1002/2017ms000936, 2017.

Matsui, H. and Mahowald, N.: Development of a global aerosol model using a two-dimensional sectional method: 2. Evaluation

and sensitivity simulations, J. Adv. Model. Earth Sy., 9, 1887–1920, https://doi.org/10.1002/2017ms000937, 2017.

Matsui, H., Hamilton, D. S., and Mahowald, N. M.: Black carbon radiative effects highly sensitive to emitted particle size when resolving mixing-state diversity, Nat. Commun., 9, 3446, https://doi.org/10.1038/s41467-018-05635-1, 2018.

Matsui, H., Mori, T., Ohata, S., Moteki, N., Oshima, N., Goto-Azuma, K., Koike, M., and Kondo, Y.: Contrasting source contributions of Arctic black carbon to atmospheric concentrations, deposition flux, and atmospheric and snow radiative effects, Atmos. Chem. Phys., 22, 8989–9009, https://doi.org/10.5194/acp-22-8989-2022, 2022.

McConnell, J. R., Edwards, R., Kok, G. L., Flanner, M. G., Zender, C. S., Saltzman, E. S., Banta, J. R., Pasteris, D. R., Carter, M. M., and Kahl, J. D. W.: 20th-century industrial black carbon emissions altered arctic climate forcing, Science, 317, 1381–1384, https://doi.org/10.1126/science.1144856, 2007.

Ming, J., Xiao, C. D., Wang, F. T., Li, Z. Q., and Li, Y. M.: Grey Tienshan Urumqi Glacier No. 1 and light-absorbing impurities, Environ. Sci. Pollut. Res., 23, 9549–9558, https://doi.org/10.1007/s11356-016-6182-7, 2016.

Mori, T., Moteki, N., Ohata, S., Koike, M., Goto-Azuma, K., Miyazaki, Y., and Kondo, Y.: Improved technique for measuring the size distribution of black carbon particles in liquid water, Aerosol Sci. Technol., 50, 242–254, https://doi.org/10.1080/02786826.2016.1147644, 2016.

Mori, T., Goto-Azuma, K., Kondo, Y., Ogawa-Tsukagawa, Y., Miura, K., Hirabayashi, M., Oshima, N., Koike, M., Kupiainen, K., Moteki, N., Ohata, S., Sinha, P. R., Sugiura, K., Aoki, T., Schneebeli, M., Steffen, K., Sato, A., Tsushima, A., Makarov, V., Omiya, S., Sugimoto, A., Takano, S., and Nagatsuka, N.: Black carbon and inorganic aerosols in Arctic snowpack, J. Geophys. Res.-Atmos., 124, 325–356, https://doi.org/10.1029/2019JD030623, 2019.

Mori, T., Kondo, Y., Ohata, S., Zhao, Y., Sinha, P. R., Oshima, N., Matsui, H., Moteki, N., and Koike. N.: Seasonal variation of wet deposition of black carbon in Arctic Alaska, J. Geophys. Res.-Atmos., 125, e2019JD032240, https://doi.org/10.1029/2019JD032240, 2020.

Mori, T., Kondo, Y., Ohata, S., Goto-Azuma, K., Fukuda, K., Ogawa-Tsukagawa, Y., Moteki, N., Yoshida, A., Koike, M., Sinha, P. R., Oshima, N., Matsui, H., Tobo, Y., Yabuki, M., and Aas, W.: Seasonal variation of wet deposition of black carbon at Ny-Ålesund. Svalbard, J. Geophys. Res.-Atmos., 126, e2020JD034110, https://doi.org/10.1029/2020JD034110, 2021.

Mori, T., Kondo, Y., Goto-Azuma, K., Moteki N., Yoshida, A., Fukuda K., Ogawa-Tsukagawa, Y., Ohata, S., and Koike, M., Measurement of number and mass size distributions of light-absorbing iron oxide aerosols in liquid water with a modified single-particle soot photometer, Aerosol Sci Technol., 57, 35–49, https://doi.org/10.1080/02786826.2022.2144113, 2023.

Mossop, S. C.: Stratospheric particles at 20 km, Nature, 199, 325–326, https://doi.org/10.1016/0016-7037(65)90017-7, 1963.

Moteki, N. and Kondo, Y.: Dependence of Laser-Induced Incandescence on Physical Properties of Black Carbon Aerosols: Measurements and Theoretical Interpretation, Aerosol Sci. Technol., 44, 663–675, https://doi.org/10.1080/02786826.2010.484450, 2010.

Murr, L. E. and Soto, K. F.: A TEM study of soot, carbon nanotubes, and related fullerene nanopolyhedra in common fuel-gas combustion sources, Mater. Charact., 55, 50–65, https://doi.org/10.1016/j.matchar.2005.02.008, 2005.

Ohata, S., Yoshida, A., Moteki, N., Adachi, K., Takahashi, Y., Kurisu, M., and Koike, M.: Abundance of light-absorbing anthropogenic iron oxide aerosols in the urban atmosphere and their emission sources, J. Geophys. Res.-Atmos., 123, 8115–8134, https://doi.org/10.1029/2018JD028363, 2018.

Ohata, S., Koike, M., Yoshida, A., Moteki, N., Adachi, K., Oshima, N., Matsui, H., Eppers, O., Bozem, H., Zanatta, M., and Herber, A. B.: Arctic black carbon during PAMARCMiP 2018 and previous aircraft experiments in spring, Atmos. Chem. Phys., 21, 15861–15881, https://doi.org/10.5194/acp-21-15861-2021, 2021.

Okada, K.: Nature of individual hygroscopic particles in the urban atmosphere, J. Meteor. Soc. Japan, 61, 727–735, https://doi.org/10.2151/jmsj1965.61.5_727, 1983.

O'Rourke, P. R., Smith, S., Mott, A., Ahsan, H. McDuffie, E., Crippa, M., Klimont, Z., McDonald, B., Wang, S., Nicholson, M., Feng, L., and Hoesly, R. M.: CEDS v_2021_04_21 Release Emission Data (v_2021_02_05), Zenodo [data set], https://doi.org/10.5281/zenodo.4741285, 2021.

Osmont, D., Wendl, I. A., Schmidely, L., Sigl, M., Vega, C. P., Isaksson, E., and Schwikowski, M.: An 800-year high-resolution black carbon ice core record from Lomonosovfonna, Svalbard, Atmos. Chem. Phys., 18, 12777–12795, https://doi.org/10.5194/acp-18-12777-2018, 2018.

Pang, Y., Chen, M., Wang, Y., Chen, X., Teng, X., and Kong, S., Morphology and fractal dimension of size-resolved soot particles emitted from combustion sources. J. Geophys. Res.-Atmos., 128, e2022JD037711, https://doi.org/10.1029/2022JD037711, 2023.

Pósfai, M., Gelencser, A., Simonics, R., Arato, K., Li, J., Hobbs, P. V., and Buseck, P. R.: Atmospheric tar balls: Particles from biomass and biofuel burning, J. Geophys. Res.-Atmos., 109, D06213, https://doi.org/10.1029/2003JD004169, 2004.

Qu, B., Ming, J., Kang, S.-C., Zhang, G.-S., Li, Y.-W., Li, C.-D., Zhao, S.-Y., Ji, Z.-M., and Cao, J.-J.: The decreasing albedo of the Zhadang glacier on western Nyainqentanglha and the role of light-absorbing impurities, Atmos. Chem. Phys., 14, 11117–11128, https://doi.org/10.5194/acp-14-11117-2014, 2014.

Ramanathan, V. and Carmichael, G.: Global and regional climate changes due to black carbon, Nat. Geosci., 1, 221–227, https://doi.org/10.1038/ngeo156, 2008.

Sachdeva, K. and Attri, A. K.: Morphological characterization of carbonaceous aggregates in soot and free fall aerosol samples, Atmos. Environ., 42, 1025–1034, 2008.

Sakakibara, D. and Sugiyama, S.: Ice-front variations and speed changes of calving glaciers in the Southern Patagonia Icefield from 1984 to 2011, J. Geophys. Res.-Earth Surf., 119, 2541–2554, https://doi.org/10.1002/2014JF003148, 2014.

Sakakibara, D. and Sugiyama, S.: Seasonal ice-speed variations in 10 marine-terminating outlet glaciers along the coast of Prudhoe Land, northwestern Greenland, J. Glaciol., 66, 25–34, https://doi.org/10.1017/jog.2019.81, 2020.

Samson, R. J., Mulholland, G. W., and Gentry, J. W.: Structural analysis of soot agglomerates, Langmuir, 3, 272–281, https://doi.org/10.1021/la00074a022, 1987.

Schwarz, J. P., Samset, B. H., Perring, A. E., Spackman, J. R., Gao, R. S., Stier, P., Schulz, M., Moore, F. L., Ray, E. A., and Fahey, D. W.: Global-scale seasonally resolved black carbon vertical profiles over the Pacific, Geophys. Res. Lett., 40, 5542–5547, https://doi.org/10.1002/2013GL057775, 2013.

Sigl, M., Abram, N. J., Gabrieli, J., Jenk, T. M., Osmont, D., and Schwikowski, M.: 19th century glacier retreat in the Alps preceded the emergence of industrial black carbon deposition on high-alpine glaciers, The Cryosphere, 12, 3311–3331, https://doi.org/10.5194/tc-12-3311-2018, 2018.

Sinha, P. R., Kondo, Y., Goto-Azuma, K., Tsukagawa, Y., Fukuda, K., Koike, M., Mori, T., Oshima, N., Førland, E. J., Irwin, M., Gallet, J.-C., and Pedersen, C. A.: Seasonal progression of the deposition of black carbon by snowfall at Ny-Ålesund, Spitsbergen, J. Geophys. Res.-Atmos., 123, 997–1016, https://doi.org/10.1002/2017JD028027, 2018.

Skiles, S. M., Flanner, M., Cook, J. M., Dumont, M., and Painter, T. H.: Radiative forcing by light-absorbing particles in snow, Nat. Clim. Change, 8, 964–971, https://doi.org/10.1038/s41558-018-0296-5, 2018.

Sterle, K. M., McConnell, J. R., Dozier, J., Edwards, R., and Flanner, M. G.: Retention and radiative forcing of black carbon in eastern Sierra Nevada snow, The Cryosphere, 7, 365–374, https://doi.org/10.5194/tc-7-365-2013, 2013.

Takeuchi, N. and Li, Z.: Characteristics of surface dust on Ürümqi Glacier No. 1 in the Tien Shan Mountains, China, Arct. Antarct. Alp. Res., 40, 744–750, https://www.tandfonline.com/doi/full/10.1657/1523-0430(07-094)[TAKEUCHI]2.0.CO;2, 2008.

The GlaMBIE Team: Community estimate of global glacier mass changes from 2000 to 2023, Nature, 639, 382–388, https://doi.org/10.1038/s41586-024-08545-z, 2025.

Ueda, S., Osada, K., and Okada, K.: Mixing states of cloud interstitial particles between water-soluble and insoluble materials at Mt. Tateyama, Japan: Effect of meteorological conditions, Atmos. Res., 99, 325–336, https://doi.org/10.1016/j.atmosres.2010.10.021, 2011a.

Ueda, S., Osada, K., and Takami, A.: Morphological features of soot-containing particles internally mixed with water-soluble materials in continental outflow observed at Cape Hedo, Okinawa, Japan, J. Geophys. Res., 116, https://doi.org/10.1029/2010JD015565, 2011b.

Ueda, S., Nakayama, T., Taketani, F., Adachi, K., Matsuki, A., Iwamoto, Y., Sadanaga, Y., and Matsumi, Y.: Light absorption and morphological properties of soot-containing aerosols observed at an East Asian outflow site, Noto Peninsula, Japan, Atmos. Chem. Phys., 16, 2525–2541, https://doi.org/10.5194/acp-16-2525-2016, 2016.

Ueda, S., Osada, K., Hara, K., Yabuki, M., Hashihama, F., and Kanda, J.: Morphological features and mixing states of soot-containing particles in the marine boundary layer over the Indian and Southern oceans, Atmos. Chem. Phys., 18, 9207–9224, https://doi.org/10.5194/acp-18-9207-2018, 2018.

Ueda, S., Mori, T., Iwamoto, Y., Ushikubo, Y., and Miura, K.: Wetting properties of fresh urban soot particles: Evaluation based on critical supersaturation and observation of surface trace materials, Sci. Total Environ., 811, 152274, https://doi.org/10.1016/j.scitotenv.2021.152274, 2022.

Ueda, S., Iwamoto, Y., Taketani, F., Liu, M., and Matsui, H.: Morphological features and water solubility of iron in aged fine aerosol particles over the Indian Ocean, Atmos. Chem. Phys., 23, 10117–10135, https://doi.org/10.5194/acp-23-10117-2023, 2023.

Ueda, S., Ohata, S., Iizuka, Y., Seki, O., Matoba, S., Matsui, H., Koike, M., and Kondo, Y.: Evaluation of sample storage methods for single particle analyses of black carbon in snow and ice: Merits and risks of glass and plastic vials for melted sample storage, Aerosol Sci. Technol., 59, 1–6, https://doi.org/10.1080/02786826.2025.2542900, 2025.

Xu, B., Cao, J., Joswiak, D., Liu, X., Zhao, H., and He, J.: Post depositional enrichment of black soot in snow-pack and accelerated melting of Tibetan glaciers, Environ. Res. Lett., 7, 014022, https://doi.org/10.1088/1748-9326/7/1/014022, 2012.

Yoshida, A., Moteki, N., Ohata, S., Mori, T., Tada, R., Waldhauserová, P. D., and Kondo, Y.: Detection of light-absorbing iron oxide particles using a modified single-particle soot photometer, Aerosol Sci. Technol., 50, 1–4, https://doi.org/10.1080/02786826.2016.1146402, 2016.

Zhang, Y., Kang, S., Cong, Z., Schmale, J., Sprenger, M., Li, C., Yang, W., Gao, T., Sillanpää, M., Li, X., Liu, Y., Chen, P., and Zhang, X.: Light-absorbing impurities enhance glacier albedo reduction in the southeastern Tibetan plateau, J. Geophys. Res.-Atmos., 122, 6915–6933, https://doi.org/10.1002/2016JD026397, 2017.

Zhang, Y., Gao, T., Kang, S., Sprenger, M., Tao, S., Du, W., Yang, J., Wang, F., and Meng, W.: Effects of black carbon and mineral dust on glacial melting on the Muz Taw glacier. Central Asia, Sci. Total Environ., 740, 140056, https://doi.org/10.1016/j.scitotenv.2020.140056, 2020.

Supplement of Atmos. Chem. Phys., 26, 3167–3184, 2026
https://doi.org/10.5194/acp-26-3167-2026-supplement
© Author(s) 2026. CC BY 4.0 License.

Atmospheric Chemistry and Physics
Open Access
EGU

Supplement of

Concentration and size distribution of black carbon over the ablation area of Potanin glacier: enrichment ability of surface weathering granular ice of water-insoluble particles with snow/ice melting

Sayako Ueda et al.

Correspondence to: Sayako Ueda (ueda.sayako.u2@f.mail.nagoya-u.ac.jp)

The copyright of individual parts of the supplement might differ from the article licence.

Table S1: BC, mineral dust, and OM mass concentrations of an ice core sample collected at st2c on 31 August 2022

Top	Bottom	BC	Dust	OM	Top	Bottom	BC	Dust	OM
[m depth]	[m depth]	[ng g^{-1}]	[mg g^{-1}]	[mg g^{-1}]	[m depth]	[m depth]	[ng g^{-1}]	[mg g^{-1}]	[mg g^{-1}]
0	0.1	-	-	0.021	2.15	2.29	-	0.002	0.007
0.1	0.15	4.3	0.000	0.060	2.29	2.43	7.4	0.000	0.000
0.15	0.205	127.2	4.375	0.217	2.43	2.54	-	0.001	0.000
0.205	0.305	4.3	0.004	0.000	2.54	2.65	-	0.000	0.000
0.305	0.395	-	0.000	0.010	2.65	2.76	4.7	0.000	0.000
0.395	0.495	3.4	0.001	0.000	2.76	2.86	16.4	0.000	0.000
0.495	0.595	-	0.001	0.009	2.86	2.97	7.2	0.050	0.009
0.595	0.695	-	0.000	0.014	2.97	3.05	2.7	0.005	0.000
0.695	0.795	-	0.001	0.000	3.05	3.145	3.4	0.002	0.000
0.795	0.895	-	0.003	0.000	3.145	3.225	5.7	0.002	0.000
0.895	0.98	5.6	0.000	0.000	3.225	3.335	1.5	0.007	0.011
0.98	1.09	-	0.001	0.000	3.335	3.445	2.8	0.000	0.000
1.09	1.2	-	0.002	0.000	3.445	3.545	-	-	-
1.2	1.32	-	0.040	0.009	3.545	3.635	-	-	-
1.32	1.42	-	0.007	0.010	3.635	3.725	-	-	-
1.42	1.51	-	0.019	0.014	3.725	3.86	5.2	0.002	0.000
1.51	1.605	-	0.000	0.000	3.86	4	-	0.000	0.009
1.605	1.705	-	0.000	0.000	4	4.105	-	0.003	0.000
1.705	1.825	-	0.000	0.009	4.105	4.215	-	0.000	0.000
1.825	1.97	-	0.062	0.009					
1.97	2.07	-	0.163	0.013					
2.07	2.15	-	0.013	0.011					

Table S2: BC, mineral dust, and OM mass concentrations of an ice core sample collected at st3c on 1 September 2022

Top	Bottom	BC	Dust	OM	Top	Bottom	BC	Dust	OM
[m depth]	[m depth]	[ng g^{-1}]	[mg g^{-1}]	[mg g^{-1}]	[m depth]	[m depth]	[ng g^{-1}]	[mg g^{-1}]	[mg g^{-1}]
0	0.13	17.3	0.150	2.395	2.17	2.27	2.6	0.000	0.000
0.13	0.23	1.3	0.000	0.000	2.27	2.37	-	0.000	0.000
0.23	0.33	-	0.000	0.000	2.37	2.47	5.1	0.000	0.001
0.33	0.43	-	0.000	0.000	2.47	2.57	12.3	0.012	0.000
0.43	0.53	1.5	0.000	0.000	2.57	2.68	-	0.011	0.000
0.53	0.63	-	0.000	0.000	2.68	2.76	3.3	0.000	0.000
0.63	0.73	-	0.010	0.000	2.76	2.86	4.3	0.000	0.002
0.73	0.83	0.1	0.000	0.003	2.86	2.975	-	0.000	0.000
0.83	0.95	3.2	0.000	0.002	2.17	2.27	2.6	0.000	0.000
0.95	1.03	-	0.000	0.001	2.27	2.37	-	0.000	0.000
1.03	1.11	4.2	0.000	0.001	2.37	2.47	5.1	0.000	0.001
1.11	1.31	-	0.000	0.001	2.47	2.57	12.3	0.012	0.000
1.31	1.41	3.7	0.012	0.000	2.57	2.68	-	0.011	0.000
1.41	1.51	3.7	0.000	0.002	2.68	2.76	3.3	0.000	0.000
1.51	1.61	2.4	0.000	0.002	2.76	2.86	4.3	0.000	0.002
1.61	1.7	3.6	0.012	0.000	2.86	2.975	-	0.000	0.000
1.7	1.79	-	0.000	0.003					
1.79	1.89	-	0.000	0.000					
1.89	1.99	-	0.000	0.000					
1.99	2.09	3.3	0.000	0.002					
2.09	2.17	1.8	0.000	0.000					

Table S3-1: Sample information and BC mass concentrations of snow, ice, and precipitation samples in summer 2023

Sample ID	Sampling date	Site	Type and sampling details		BC [ng g^{-1}]
BC23#02	2023/6/30	st2c	surface water		4.0
BC23#03	2023/7/1	st5r	surface snow		5.9
BC23#04	2023/7/1	Base camp	snow	7/1 16:00–20:00	3.2
BC23#05	2023/7/2	Base camp	snow	7/1 20:00 – 7/2 5:00	2.2
BC23#06	2023/7/3	st2c	surface snow	0–2 cm 225 cm^2	6.9
BC23#07	2023/7/3	st2c	granular ice	2–4 cm 225 cm^2	32.2
BC23#08	2023/7/3	st2c	surface snow	0–3 cm 225 cm^2	8.8
BC23#09	2023/7/3	st2c	granular ice	3–5 cm 225 cm^2	18.1
BC23#10	2023/7/3	st2c	surface snow	0–2 cm 400 cm^2	22.7
BC23#11	2023/7/3	st2c	granular ice	2–4 cm 400 cm^2	29.7
BC23#12	2023/7/8	ACC	melt forms	0–10.5 cm	5.4
BC23#13	2023/7/8	ACC	rounded grains	10.5–17.0 cm	10.2
BC23#14	2023/7/8	ACC	water-bearing layer & melt forms	17.0–20.0 cm	3.7
BC23#15	2023/7/8	ACC	ice layer & melt forms	20–24 cm	84.0
BC23#16	2023/7/10	Base camp	rain	7/9/19:40–7/10 7:00	6.1
BC23#17	2023/7/12	st5r	surface water		2.7
BC23#18	2023/7/12	st4c	surface water		7.1
BC23#19	2023/7/14	st2c	surface water		8.4
BC23#20	2023/8/5	st2c	surface water		1.8

Table S3-2: Sample information and BC mass concentrations of snow, ice, and precipitation samples in summer 2023

Sample ID	Sampling date	Site	Type and sampling details		BC [ng g^{-1}]
BC23#21	2023/8/5	st2c	surface water		6.4
BC23#22	2023/8/7	Base camp	rain	8/7 7:15–16:30	3.1
BC23#23	2023/8/8	st5r	surface water		10.9
BC23#24	2023/8/8	st4c	surface water		3.2
BC23#25	2023/8/8	st5r	surface ice	84 cm^2, 36 g	555.1
BC23#26	2023/8/8	st4c	surface ice	110 cm^2, 55.5 g	159.1
BC23#27	2023/8/9	st3c	surface water		7.2
BC23#28	2023/8/11	Base camp	rain	8/11 8:40–10:00	1.8
BC23#29	2023/8/12	st2c	surface water		4.0
BC23#30	2023/8/12	st2c	surface ice	100 cm^2, 62.2 g	42.0

Table S4-1: Sample information and BC mass concentrations of snow, ice, and precipitation samples in summer 2024

Sample ID	Sampling date	Site	Type		Surface granular ice thickness [cm]	BC [ng g^{-1}]
BC24#01	2024/7/22	st2c	surface ice	dark	1	38.5
BC24#02	2024/7/22	st2c	surface ice	dark	1.5	16.5
BC24#03	2024/7/22	st2c	surface ice	dark	1.45	96.4
BC24#04	2024/7/22	st2c	surface ice	white	2.25	16.4
BC24#05	2024/7/22	st2c	surface ice	white	2.125	10.3
BC24#06	2024/7/22	st2c	surface ice	white	1.25	8.4
BC24#08	2024/7/22	st2c	surface ice for experiment	meltwater		15.4
BC24#09	2024/7/22	st2c		residual snow		4.5
BC24#10	2024/7/24	st2c	surface ice		2	47.5
BC24#11	2024/7/24	st2c	surface ice		1.175	179.6
BC24#12	2024/7/24	st2c	surface ice		3.375	92.9
BC24#13	2024/7/24	st2c	surface ice		1.75	44.5
BC24#14	2024/7/26	st5r	surface ice	dark	2.5	600.7
BC24#15	2024/7/26	st5r	surface ice	dark	1.875	269.7
BC24#16	2024/7/26	st5r	surface ice	dark	1.25	184.2
BC24#17	2024/7/26	st5r	surface ice	dark	2.25	134.0
BC24#18	2024/7/26	st5r	surface ice	dark	4.5	255.5
BC24#19	2024/7/26	st5r	surface ice	white	7.5	17.1
BC24#20	2024/7/26	st5r	surface ice	white	2.75	41.3
BC24#21	2024/7/26	st5r	surface ice	white	2	379.1
BC24#22	2024/7/26	st5r	surface ice	white	2.5	56.9
BC24#23	2024/7/26	st5r	surface ice	white	2	71.3
BC24#24	2024/7/27	st4c	surface ice	dark	0.75	38.5

Table S4-2: Sample information and BC mass concentrations of snow, ice, and precipitation samples in summer 2024

Sample ID	Sampling date	Site	Type and sampling details		Surface granular ice thickness [cm]	BC [ng g^{-1}]
BC24#25	2024/7/27	st4c	surface ice	dark	0.75	115.5
BC24#26	2024/7/27	st4c	surface ice	dark	5	37.9
BC24#27	2024/7/27	st4c	surface ice	dark	3.625	56.6
BC24#28	2024/7/27	st4c	surface ice	dark	2.25	31.2
BC24#29	2024/7/27	st4c	surface ice	white	2.875	16.7
BC24#30	2024/7/27	st4c	surface ice	white	3.375	45.5
BC24#31	2024/7/27	st4c	surface ice	white	1.75	28.9
BC24#32	2024/7/27	st4c	surface ice	white	1.75	40.9
BC24#33	2024/7/27	st4c	surface ice	white	1.375	39.3
BC24#34	2024/7/30	st3c	surface ice	dark	3.75	46.8
BC24#35	2024/7/30	st3c	surface ice	dark	2.75	24.7
BC24#37	2024/7/30	st3c	surface ice	dark	2.75	124.2
BC24#38	2024/7/30	st3c	surface ice	dark	1.625	31.2
BC24#39	2024/7/30	st3c	surface ice	white	3.625	56.7
BC24#41	2024/7/30	st3c	surface ice	white	1.25	25.2
BC24#42	2024/7/30	st3c	surface ice	white	1.125	22.6
BC24#43	2024/7/30	st3c	surface ice	white	0.75	20.6
BC24#44	2024/8/1	ACC	aged snow			48.2
BC24#45	2024/8/1	ACC	aged snow			443.5
BC24#46	2024/8/1	st2c	surface ice	dark	0.875	55.0
BC24#47	2024/8/2	st2c	surface ice	dark	1.625	15.9
BC24#48	2024/8/2	st2c	surface ice	dark	1.5	36.5
BC24#49	2024/8/2	st2c	surface ice	dark	1	7.7

Table S5: Annual BC deposition flux calculated using CAM-ATRAS

Year	BC flux [ng cm^{-2} $year^{-1}$]
2014	1495
2015	1439
2016	1298
2017	1193
2018	1297
2019	1178
2020	1216
2021	1352
2022	896
2023	1435

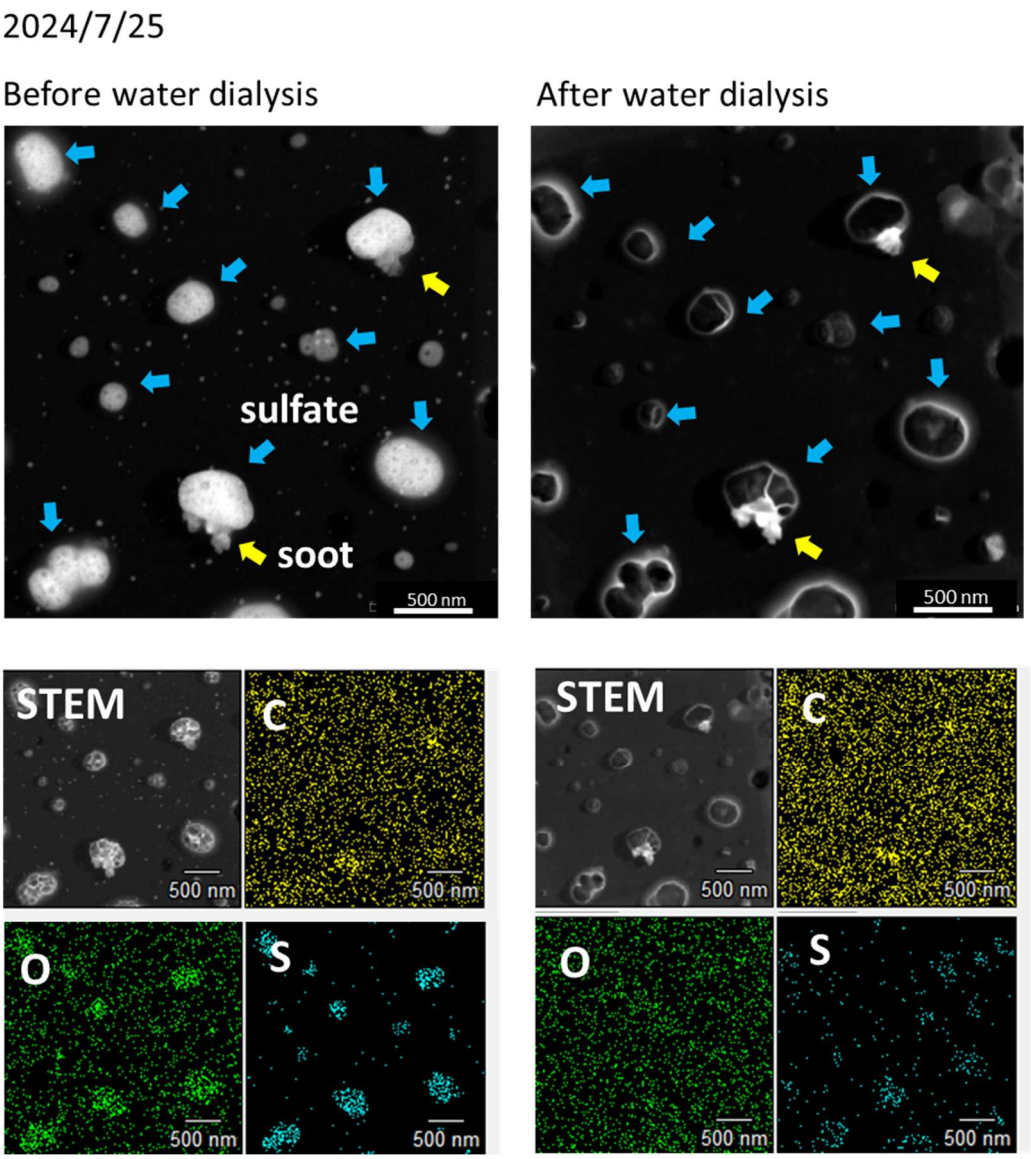

Figure S1: STEM images and elemental maps of atmospheric aerosol samples collected on 25 July 2024. The aerosol samples were collected at Base camp during 12:58–13:08 using a two-stage cascade impactor at a 0.8 L min^{-1} flow rate. The 50% cutoff diameters of the first and second stages are, respectively, 0.3 and 1.0 μm at 1 atm. The photograph is for the second stage. The condition was slight rain.

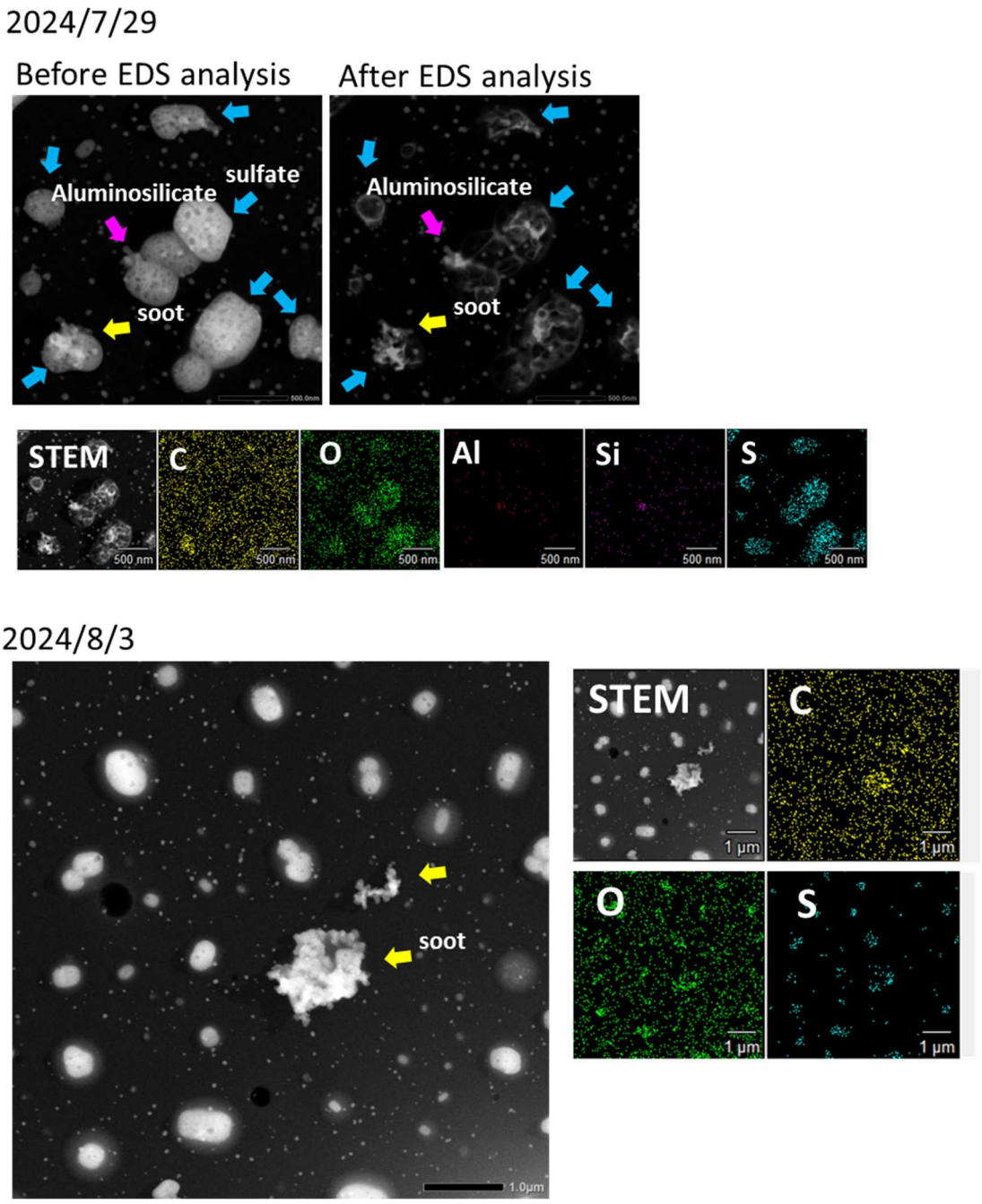

Figure S2: STEM images and elemental maps of atmospheric aerosol samples collected at Base Camp in 2024. Aerosol samples were collected during 17:50–18:02 on 29 July and during 7:57–8:10 on 3 August respectively under fine, windy conditions and fine, weak-wind conditions.

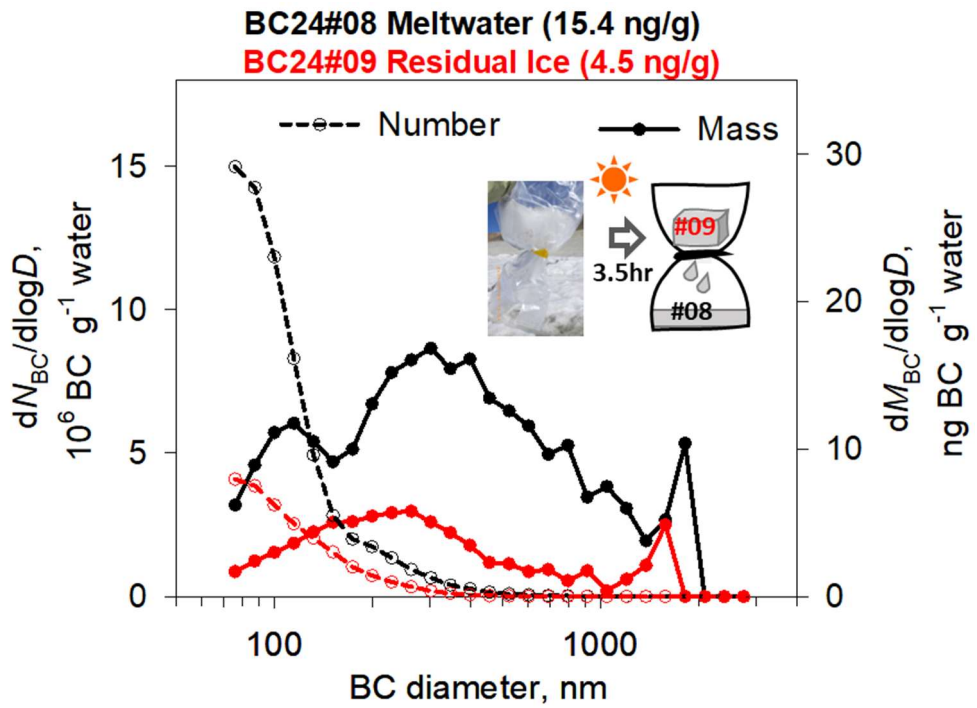

Figure S3: Number–size and mass–size distributions of BC for meltwater and residual ice originating from a surface ice sample.